USGS
science for a changing world

Coastal and Marine Hazards and Resources Program

Comparisons of Shoreline Positions from Satellite-Derived and Traditional Field- and Remote-Sensing Techniques

Open-File Report 2025–1054

U.S. Department of the Interior
U.S. Geological Survey

Comparisons of Shoreline Positions from Satellite-Derived and Traditional Field- and Remote-Sensing Techniques

By Andrea C. O'Neill, Sharon F. Batiste, Daniel D. Buscombe, Joseph Burgess, Kara S. Doran, Ann E. Gibbs, Rachel E. Henderson, Julia L. Heslin, Catherine N. Janda, Mark A. Lundine, Joseph F. Terrano, Jonathan A. Warrick, and Kathryn M. Weber

Coastal and Marine Hazards and Resources Program

Open-File Report 2025–1054

U.S. Department of the Interior
U.S. Geological Survey

U.S. Geological Survey, Reston, Virginia: 2025

Suggested citation:
O'Neill, A.C., Batiste, S.F., Buscombe, D.D., Burgess, J., Doran, K.S., Gibbs, A.E., Henderson, R.E., Heslin, J.L., Janda, C.N., Lundine, M.A., Terrano, J.F., Warrick, J.A., and Weber, K.M., 2025, Comparisons of shoreline positions from satellite-derived and traditional field- and remote-sensing techniques: U.S. Geological Survey Open-File Report 2025–1054, 41 p., https://doi.org/10.3133/ofr20251054.

ISSN 2331-1258 (online)

Contents

Figures

Tables

Conversion Factors

U.S. customary units to International System of Units

Multiply	By	To obtain
	Length	
inch (in.)	2.54	centimeter (cm)
inch (in.)	25.4	millimeter (mm)
foot (ft)	0.3048	meter (m)
mile (mi)	1.609	kilometer (km)
mile, nautical (nmi)	1.852	kilometer (km)
yard (yd)	0.9144	meter (m)
	Area	
acre	4,047	square meter (m^2)
acre	0.004047	square kilometer (km^2)
square mile (mi^2)	259.0	hectare (ha)
	Volume	
cubic yard (yd^3)	0.7646	cubic meter (m^3)
	Mass	
ton, short (2,000 lb)	0.9072	metric ton (t)

International System of Units to U.S. customary units

Multiply	By	To obtain
	Length	
centimeter (cm)	0.3937	inch (in.)
millimeter (mm)	0.03937	inch (in.)
meter (m)	3.281	foot (ft)
kilometer (km)	0.6214	mile (mi)
kilometer (km)	0.5400	mile, nautical (nmi)
meter (m)	1.094	yard (yd)
	Area	
square meter (m^2)	0.0002471	acre
square kilometer (km^2)	247.1	acre
hectare (ha)	0.003861	square mile (mi^2)
	Volume	
cubic meter (m^3)	1.308	cubic yard (yd^3)
	Mass	
metric ton (t)	1.102	ton, short (2,000 lb)

Datums

Vertical coordinate information is referenced to multiple datums, including the mean sea level (MSL) and mean high water (MHW) datums for Barter Island, Alaska; Cape Cod, Massachusetts; Elwha River, Washington; Madeira Beach, Florida; and Rincón, Puerto Rico.

Horizontal coordinate information is referenced to the North American Datum of 1983 (NAD 83).

Elevation, as used in this report, refers to distance above the vertical datum specified.

Supplementary Information

Meters per pixel (m/px) is the spatial resolution of satellites, denoting the smallest observable detail within the satellite image itself.

Abbreviations

GeoJSON	Geographical JavaScript Object Notation
GNSS	Global Navigation Satellite System
IQR	interquartile range
L5	Landsat 5
L7	Landsat 7
L8	Landsat 8
L9	Landsat 9
LOESS	locally estimated scatterplot smoothing
MAE	mean absolute error
MAPE	mean absolute percentage error
ME	mean error
MHW	mean high water
ML	machine learning
MLW	mean low water
MNDWI	Modified Normalized Difference Water-Index
NIR	near-infrared
RMSE	root mean squared error
RMSPE	root mean squared percentage error
ROI	region of interest
SDS	satellite-derived shorelines
SWASH	Surveying Wide-Area Shorelines
SWIR1	shortwave infrared
USGS	U.S. Geological Survey

Comparisons of Shoreline Positions from Satellite-Derived and Traditional Field- and Remote-Sensing Techniques

By Andrea C. O'Neill, Sharon F. Batiste, Daniel D. Buscombe, Joseph Burgess, Kara S. Doran, Ann E. Gibbs, Rachel E. Henderson, Julia L. Heslin, Catherine N. Janda, Mark A. Lundine, Joseph F. Terrano, Jonathan A. Warrick, and Kathryn M. Weber

Abstract

Satellite-derived shorelines (SDS) have the potential to help researchers answer critical coastal science questions and support work to predict coastal change by filling in the spatial and temporal gaps present in current field-based and remote-sensing data collection methods. The U.S. Geological Survey conducted comparison analyses of traditionally sourced shorelines and SDS in diverse coastal landscapes to determine how SDS could be used in ongoing and future work across varied coastal environments and provided some initial findings that could be used for implementation. Using CoastSeg, a browser-based program for SDS detection and mapping, SDS for the period 1984–2023 for multiple locations across the United States were compared to shoreline positions from traditionally sourced shoreline data. In this report, the authors present these comparisons alongside lessons learned and challenges encountered when building SDS workflows in different coastal locations. Results show that individual SDS have larger uncertainty and yet produced similar linear trends to sparser, traditionally sourced shoreline data; because SDS methods provide orders of magnitude more data than traditional shoreline-detection methods, they can be used to evaluate shoreline behaviors. Refining average scalar slopes used in tidal corrections did not result in substantial decreases in uncertainty. Using lessons from this work to outline needs for regional implementation, initial setup time would be considerable, being on the order of weeks. However, once complete, shoreline detections and analyses are fast (on the order of minutes to hours) and achievable using a desktop computer.

1.0. Introduction

Most shoreline change information derived from traditional techniques, such as historical maps, aerial imagery, or beach surveys, is temporally sparse and does not resolve effects of significant events like storms or wave events (Thieler and others, 2007). In contrast, earth-observing satellite imagery with spatial resolutions on the order of one to tens of meters offers an efficient means for capturing the dynamics of shorelines with daily to weekly frequency over several decades (Vos and others, 2019a, b; Vitousek and others, 2023a). In addition, automated feature extraction from satellite imagery allows for a relatively rapid analysis of very large regions compared to traditional methods.

Given the global coverage and widespread public availability of decades worth of satellite imagery, satellite-derived shorelines (SDS) have the potential to provide shoreline data over large regional scales (hundreds of kilometers) and timescales of weeks to decades. SDS data can be extracted from imagery at the resolution necessary to investigate storm events and other episodic influences, even for remote locations (Warrick and others, 2022, 2023, 2025), and can inform projections of the potential effects of future shoreline hazards (Vitousek and others, 2023b) on coastal populations and resources.

Several SDS methodologies with a range of approaches have been proposed, including methods that provide annual rates without correcting for water level (Luijendijk and others, 2018), open-source methods that provide annual shorelines corrected for water level (Bishop-Taylor and others, 2021), and open-source methods that provide so-called "instantaneous" shorelines, corrected for water level, from every usable satellite image (Vos and others, 2019b; Almeida and others, 2021; Mao and others, 2021; Fitzpatrick and others, 2024a, b). Of these, CoastSat (Vos and others, 2019b) has been frequently used to study a diverse set of beach settings throughout the world (Castelle and others, 2021, 2024; Konstantinou and others, 2023; Vos and others, 2023; Muir and others, 2024; Janda and others, 2025). Evaluating SDS methodologies and the uncertainties in the datasets they generate is essential to improving coastal monitoring efforts (Vos and others, 2023). Spatial resolution and accuracy of SDS differs from traditionally sourced data; Vos and others (2023) have shown that a timeseries of shorelines can be automatically extracted from publicly available imagery with an average accuracy of approximately 10 meters (m), compared to accuracies of less than 1 m for lidar or Global Navigation Satellite System (GNSS) surveying techniques

(List and others, 2006; Farris and others, 2018). However, the study from Vos and others (2023) compared SDS with in situ shorelines at only four sites frequently used in coastal studies (Duck, North Carolina; Truc Vert, France; Torrey Pines, California; and Narrabeen, Australia) that are all sandy, wave-dominated sites with modest coastal change. To appropriately leverage these advancements across the United States, a better understanding of how these tools operate and how the reliability and uncertainty of results vary across different wave and tide regimes, beach morphologies, and coastal landscapes beyond the small number of aforementioned intensively studied "super site" sandy beaches is needed (Turner and others, 2016; Ludka and others, 2019; Hoover and others, 2024).

Systematic and random errors in SDS also occur despite advancements in automated waterline detection from satellite imagery, water level correction, and mapping the shoreline intersection with shore-normal transects. These errors arise from a combination of factors that vary by location: (a) water-level variability because of tide, surge, setup, and swash; (b) image degradation because of haze, cloud, blur, or missing data; (c) insufficient spectral and (or) spatial resolution to accurately define the waterline; (d) beach slope variability; and (e) image misalignment because of poor georeferencing. Because of these errors, outlier detection and removal are difficult, and there is little consensus on how to improve the results. This is hindered by the fact that efforts to evaluate SDS accuracy rely on comparisons with ground-truth data, which are limited to accessible coastlines and available in relatively few locations. Additionally, the degree of certainty on applying SDS to various short-term timescales at these locations is not well constrained.

An effort bringing together a working group of coastal scientists, data users, and tool developers across the U.S. Geological Survey (USGS) Coastal and Marine Hazards and Resources Program was established to address and improve understanding of how SDS technology, methodology, results, and uncertainties vary across different coastal environments. As part of this effort, the team collaborated on the development of CoastSeg (Fitzpatrick and others, 2024a, b), a browser-based program for SDS detection and mapping, by beta testing, offering feedback, and proposing enhancements that improved the tool's usability and effectiveness across diverse coastal settings.

The goals of this effort were as follows:

- understand how well existing shoreline mapping workflows function across diverse and understudied coastal landscapes and conditions (for example, barrier islands, deltas, low-energy clastic beaches, microtidal to macrotidal conditions, and so on),
- understand factors that can contribute to per-image shoreline positional uncertainty,
- quantify the amount of time and tunable parameter adjustments required for reliable results or output,
- understand the workflow and components needed for consistent and quality output, and
- quantify the temporal and spatial scales of coastal change the resulting data can reliably characterize across these landscapes.

As an author team, we generated an SDS dataset (Buscombe and others, 2025) from diverse coastal landscapes to support the above goals. The results from this effort, including estimations of the amount of time and computation required to produce reliable SDS results, are included in this manuscript and will help to inform how the SDS workflow might be used at regional scales with other coastal science tools, resources, and data. It is our intention that lessons and shoreline mapping workflows from this work can be integrated into existing USGS work to improve the coastal science community's understanding of coastal change.

2.0. Background

SDS differ from traditionally generated shorelines, including datum-based and manually digitized shorelines, in many ways. Datum-based shorelines are derived from lidar or other elevation data sources, representing a vertical datum, such as mean sea level (MSL). SDS are proxy-based shorelines representing the land-water interface in imagery and thus are strongly influenced by the water level and wave conditions at the time of collection. Proxy-based shorelines visually define the shoreline position from aerial or satellite imagery using proxy variables like the instantaneous land-water interface, high-water line, or wet-dry line. Tidal corrections are usually implemented to adjust resulting SDS positions based on predicted astronomic water levels (Vos and others, 2019a, b; Vitousek and others, 2023a) but typically do not include corrections for wave-driven water level variations on beaches, including wave setup and swash oscillations (runup). Adjusting shoreline position to account for these wave-driven water level variations in SDS and other proxy-based shorelines is possible using a proxy-datum bias correction (Ruggiero and List, 2009). Although applying the proxy-datum bias decreases the offset between proxy- and datum-based shorelines, applying this correction to the SDS in this report was beyond the scope of this work. Refer to section 4.0 for more discussion.

SDS also differ from shorelines manually digitized from imagery, which are also influenced by the water level. Manually digitized shorelines are fully supervised, leading to trustworthy and accurate datasets if water levels and other biases are correctly accounted for (Crowell and others, 1991; Moore, 2000; Ruggiero and List, 2009). In contrast, SDS is a fully automated process, and although classification tools and machine-learning (ML) methods are constantly improving, the resulting datasets contain more noise, or fluctuations in the image and data that can distort or skew any derived results.

Similar differences can occur between manually digitized and datum-based shorelines, depending on the source imagery and transect resolution.

Many SDS techniques leverage a transect-based approach that uses shore-normal transects to constrain the classification and resulting shoreline identification. Results are usually output as shoreline positions along each transect. We adopt the same workflow for this study.

There are currently two implementations of the CoastSat workflow: the original toolbox (Vos and others, 2019b) and the re-implementation of the workflow within the CoastSeg platform. CoastSeg (Fitzpatrick and others, 2024a, b) is an extendable hub for SDS workflows and, at the time of writing, has two separate workflows for shoreline mapping: the CoastSat workflow and another workflow that uses deep learning. CoastSeg offers numerous accessibility improvements, such as "sessions" users can share and collaborate over, an intuitive graphical interface with improved tidal correction and image downloading routines, and scripts and auxiliary tools for data management, format conversion, post-processing, and other miscellaneous tasks. For this study, we used the re-implementation of the CoastSat workflow within the CoastSeg platform (henceforth, CoastSeg:CoastSat). The new "sessions" functionality allowed us to distribute analysis and quality-check tasks across the various sites and a team of users.

The accuracy of shorelines and shoreline change rates generated from the CoastSeg:CoastSat workflow, as compared with in situ shoreline data, is our primary concern. Also of interest are accessibility and repeatability of workflows, which are informally assessed. Finally, in this study, we aim to understand the scalability of these workflows to large regions of coast with little to no in situ data for calibration and validation purposes. In conjunction with previous validation results representing various coastal environments (Castelle and others, 2021; Konstantinou and others, 2023; Vos and others, 2023), we aim to map complex, dynamic shorelines using SDS to better understand the advantages and disadvantages of large-scale automated shoreline extraction and analyses for a greater part of the spectrum of the Nation's coastal environments.

In this study, the term "SDS" refers to automatically derived shoreline data using the CoastSeg:CoastSat. Traditionally sourced shorelines from various data sources and methods outlined above (including lidar, GNSS, and manually digitized shorelines from imagery) are referred to as "in situ" data.

3.0. Study Sites

The USGS conducts research supporting communities, organizations, and other state and Federal agencies in diverse coastal landscapes across the Nation. Therefore, the tools that are used to study coastal change must function in a wide range of environments. As such, the study sites in this effort span a range of tidal conditions, sediment morphological classes, and different geographical regions (fig. 1; table 1). In total, they represent a broad variety of environments where coastal research is actively conducted and ongoing information on shoreline change is needed.

3.1. Barter Island

Barter Island (fig. 2) is on northern Alaska's Beaufort Sea coast and the boundary of the U.S. Arctic National Wildlife Refuge; it contains a highly dynamic barrier system and permafrost bluffs fronting the Alaska Native community of Kaktovik and Clear Space Force Station. The sand and gravel barrier islands trend roughly east-west in the region and can be overwashed or breached during high wave or water level events. The central 3 kilometers (km) of Barter Island's northern coast is comprised of eroding coastal permafrost bluffs, mostly fronted by narrow (less than 20 m) sand and gravel beaches.

Most morphological change along this microtidal coast occurs during the ice-free months, typically July to October. The surface permafrost also thaws during these months. During this open-water season, atmospheric low-pressure systems can bring high winds, storm surges, and waves (Erikson and others, 2020). The region is also predominantly cloudy, which limits usable satellite imagery, particularly during these storm events. Because wave energy is limited to the short open-water season and is relatively lower than lower-latitude coasts, the magnitude of littoral transport is thought to be low (Hopkins and Hartz, 1978). The area has a mean diurnal tidal range of 18 centimeters (cm; National Oceanic and Atmospheric Administration, 2025), though local winds and storm systems can change water levels by several meters.

Barter Island was selected for this study because it is one of the few locations in the Arctic where a relative abundance of historical imagery exists, including very-high resolution (less than 5 m ground sample distance) satellite and aerial photography on a near annual basis since 2000. Historical shoreline and bluff positions were delineated manually (Gibbs and others, 2021) from a combination of historical maps, aerial photography, declassified satellite photography, and very-high resolution satellite imagery for a dataset of morphological evolution of Barter Island and its neighboring barrier islands (Gibbs and others, 2019a, 2020). For this study, 19 in situ shorelines were available for comparison with the SDS.

3.2. Cape Cod

Cape Cod (fig. 3), located in southeast Massachusetts, has a relatively recent geologic history; the retreat of the Laurentide ice sheet and subsequent rise in sea level began roughly 18,000 years before present (U.S. Geological Survey, 1976). The open-ocean Atlantic coast of Cape Cod

Figure 1. Maps of five study sites spread across the conterminous United States, Alaska, and the Island of Puerto Rico and descriptions of each site's coastal setting. All photographs by the U.S. Geological Survey.

(the "outer Cape") includes Cape Cod National Seashore and Monomoy National Wildlife Refuge, where a variety of ecosystems can be found (Schwarzman, 2002).

The approximately 65 km of shoreline in Cape Cod National Seashore is composed of dune-backed beaches in the north (where the dunes can be more than 25 m tall), high bluffs (as high as 30 m) fronted by narrow beaches along the central section, and barrier islands and spits in the south. There are no rivers supplying sediment to the beaches of the outer Cape; all beach sediment is derived from the eroding bluffs. There are also no coastal engineering structures along the shores of the National Seashore, making it an entirely natural littoral system. Grain size ranges from medium sand in the south to very coarse sand at the northern spit (Fisher and Leatherman, 1987). Longshore sediment transport is bi-directional, and a nodal point is near the Wellfleet-Eastham border, south of the study area (Berman, 2011; Giese and others, 2011). North of this nodal point, longshore sediment transport flows from south to north. South of the point, it flows in from north to south.

Outer Cape Cod (the outer Cape) has a semidiurnal tidal regime with a range of 2 to 3 m and a dominant east-northeast wave direction. The outer Cape is a storm-dominated coast affected by extratropical cyclones (nor'easters) and, less frequently, hurricanes. Long-term (about 100 years) shoreline-change rates, which were derived from historical maps and imagery and modern lidar data, show an overall erosional trend for most of the outer Cape, whereas short-term (about 30 years) trends show more variable patterns (Hapke and others, 2011).

Table 1. Details for each location used in a comparison study of shoreline positions determined using satellite-derived and traditional field- and remote-sensing techniques.

[Tide ranges are microtidal unless otherwise indicated. km, kilometer; m, meter; U.S., United States]

Location	Region	Observation record (in situ shorelines)				Location details		
		Dates of record	Number compared shorelines[1]	Coast length[2] (km)	Source	Sediment, slope, and morphology	Mean tide range (m)	Extraction challenges[3]
Barter Island	Alaska	1987–2020	12	17	Gibbs and others, 2020	Sand and gravel (coarse-mixed), shallow slope, barrier islands, bluff-backed beaches	0.1	Ice, weather and clouds, narrow beaches fronting bluffs, adjacent marsh and wetlands, large coastline changes
Cape Cod	U.S. Northeast, Massachusetts	1998–2005	59	9.5	Farris and others, 2020	Sand (medium to very coarse), medium-steep slope, dune and bluff-backed beach	[4]2.5	Weather and clouds, welded bars, longshore bars and troughs, breaking waves
Elwha River delta	U.S. Northwest, Washington	2009–24	138	8.5	Stevens and others, 2017; Miller, 2025	Coarse-grained gravel, mixed slope, river delta	[4]2.15	Complex beach morphology (bars, narrow berms), gravel beach
Madeira Beach	U.S. Southeast, Florida	2016–23	23	0.6	Brown and others, 2018	Sand (medium), low dune and berm beach	0.8	Weather, clouds, managed beach
Rincón	Puerto Rico	1987–2018	2	5.5	Henderson and others, 2021	Sand (medium), mixed slope, coral reef-fronted beaches	0.4	Complex nearshore bathymetry, coral reefs, weather and clouds

[1]Number of traditionally sourced in situ shorelines that coincided with satellite imagery (±10 days).

[2]Refers to the alongshore length of coast in the observed shoreline record used in this analysis.

[3]Describes the various complications with shoreline extraction at each location.

[4]Location is mesotidal.

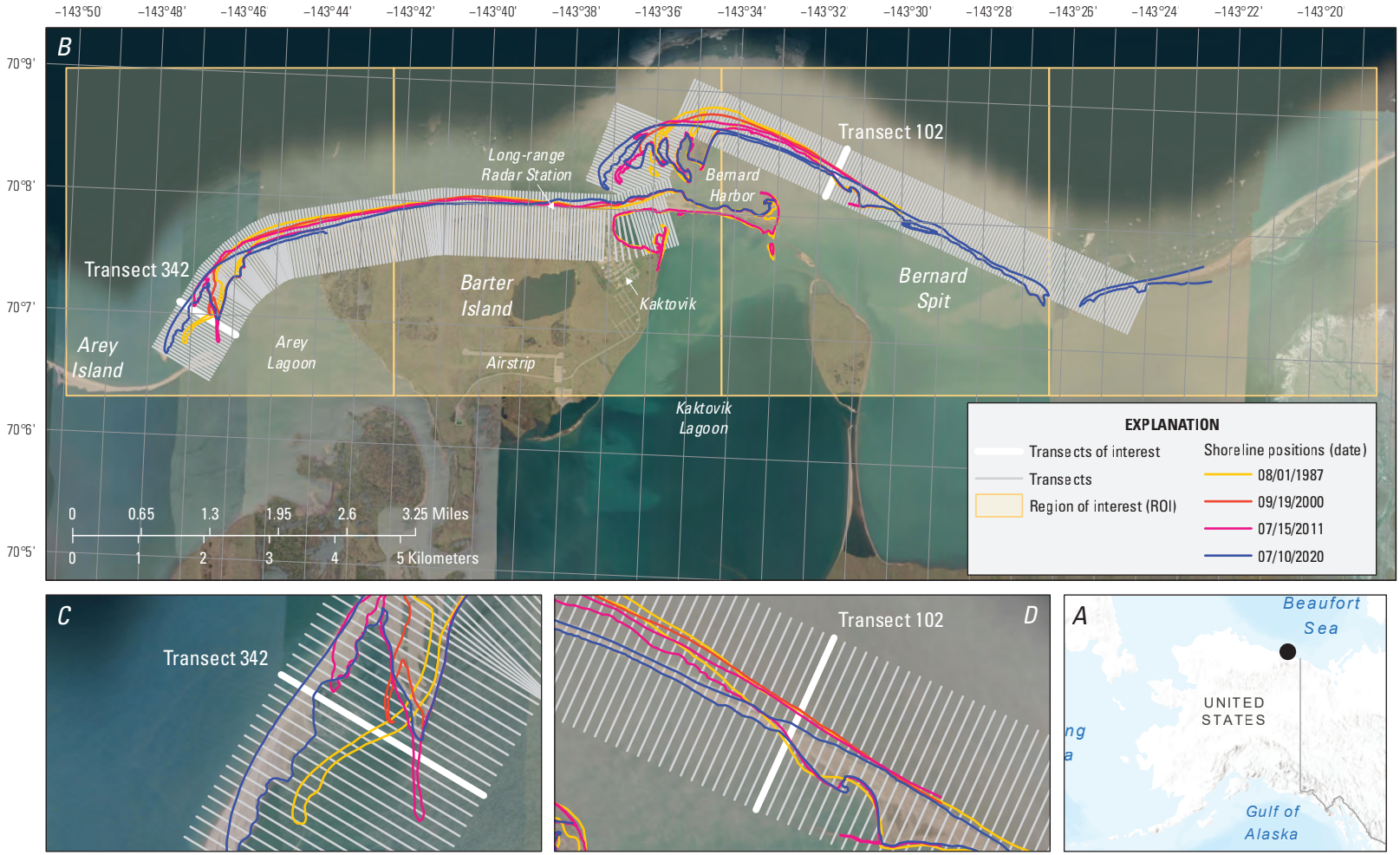

Shoreline positions from Gibbs and others (2020)
Base for all maps from Esri and its licenses, copyright 2025
Universal Transverse Mercator, zone 7 north
North American Datum of 1983

Figure 2. Historical shoreline positions for Barter Island and neighboring Bernard Spit and Arey Island, Alaska, 1987–2020: *A*, study area location; *B*, site view with regions of interest (ROIs), transects, and representative traditionally sourced in situ shorelines; *C*, detailed view of transect 342 on Barter Island's western side showing evolution of barrier spit; and *D*, detailed view of transect 102 at Bernard Spit showing retreat between 1987 and 2020.

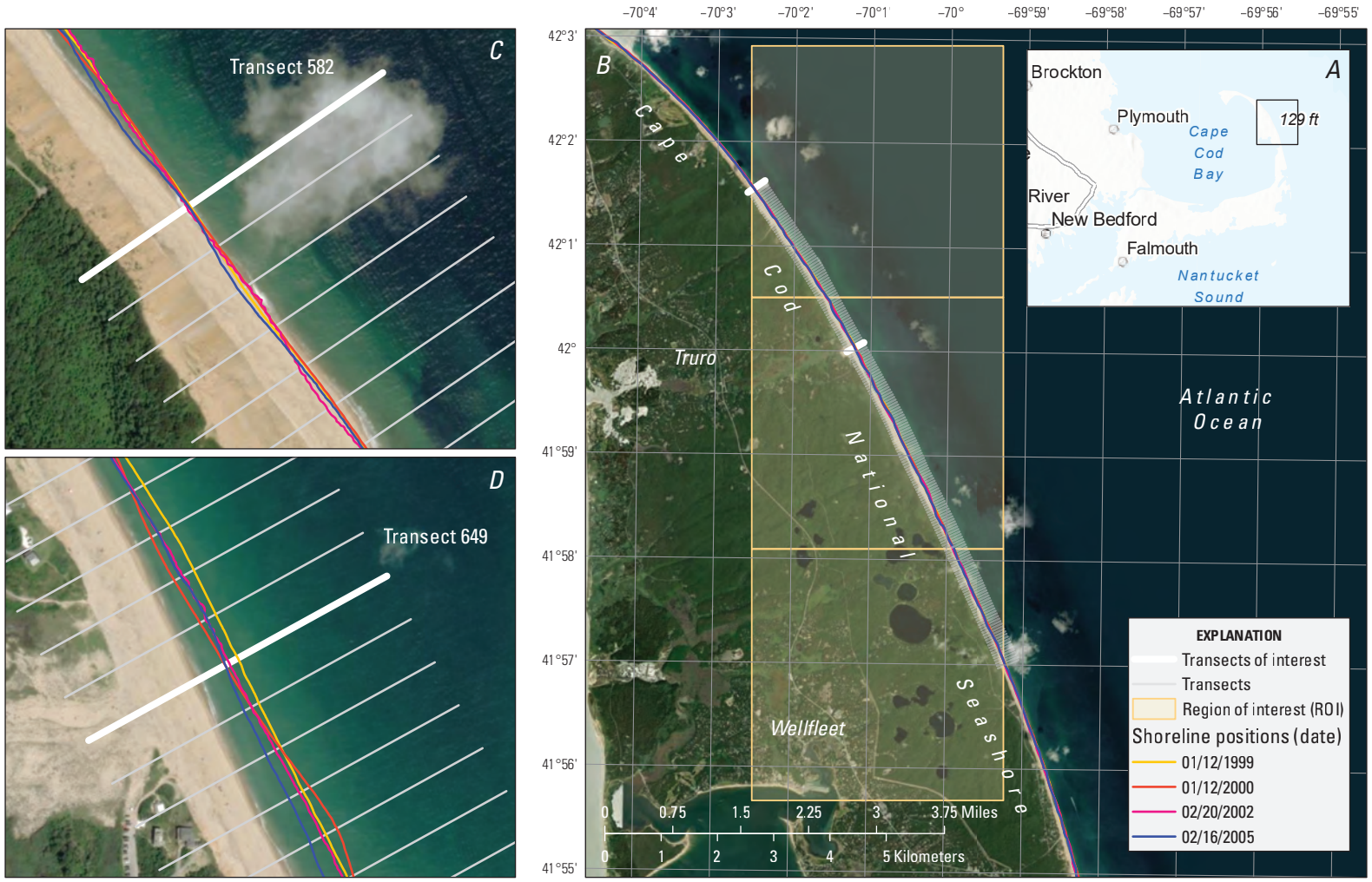

Shoreline positions from Farris and others (2020)
Base for all maps from Esri and its licenses, copyright 2025
Universal Transverse Mercator, zone 19 north
North American Datum of 1983

Figure 3. Historical shoreline positions for Cape Cod, Massachusetts, 1995–2005: *A*, study area location; *B*, site view with regions of interest (ROI), transects, and representative traditionally sourced in situ shorelines; and detailed views of *C*, transect 582 and *D*, transect 649.

Cape Cod National Seashore was selected for this study because of the large in situ dataset available for comparison with the SDS. Between 1998 and 2005, an intensive USGS field program was conducted along 45 km of the outer Cape, from Nauset Inlet in the south to Race Point in the north (Farris and others, 2020). A ground-based all-terrain vehicle system called SWASH (Surveying Wide-Area Shorelines) was equipped with GPS sensors and was used to traverse a single, shore-parallel line along the foreshore to collect horizontal and vertical position and beach slope. The shoreline position was determined by extrapolating from the driven track to the mean high water (MHW) elevation. Over the 7 years the field program was active, 111 shoreline surveys were conducted. Most of these were biweekly, but several pre-storm, post-storm, and recovery triplet surveys were also performed. A 9.5 km alongshore subset of this dataset is used for comparison with the SDS.

3.3. Elwha River Delta

The Elwha River delta (fig. 4) and its corresponding littoral system lie within the Strait of Juan de Fuca in the northern part of the State of Washington. The littoral cell is roughly 20 km long and ends at a terminal spit. The Elwha River encompasses an 831-square-kilometer (km^2) watershed that drains the interior of the Olympic Mountains (Warrick and others, 2009). Its beaches are characterized by a steep, reflective foreshore backed by a berm with a foreshore slope between 0.1 and 0.2. East of the river mouth, the Elwha River delta beach includes a flat low-tide terrace that generally has a grain size of gravel to cobble with slopes of about 0.02. Sediment in the region is categorized as mixed sand and gravel with a mean grain size of roughly 40 millimeters. Significant wave heights within the region are usually less than 1 m, and tides are diurnal with a range of 2.22 m between the mean lower low water and mean higher high water (Warrick and others, 2019). Surveys in the area between 2004 and 2007 have shown that most of the erosion occurs in the winter (November through March) with lower rates of change in the summer (June through August) (Warrick and others, 2009).

Beaches near the delta are placed into two morphological units defined by their location east and west of the river mouth. East of the river mouth, beaches are characterized by a gravel low-tide terrace, mixed sand and gravel foreshore, and a low berm. This area has also seen periods of high erosion, especially from 1939 to 2006. Beaches west of the river mouth have been much more stable and have a high berm and no subaerial low-tide terrace like the eastern portion (Warrick and others, 2009; Miller and others, 2011). Because of the relatively steep beaches around the delta, waves break directly onto the beach, which limits the width of the surf zone. Alongshore transport is greater along the middle and eastern sides of the delta because waves approach at an angle of roughly 265 degrees (Miller and others, 2011; Gelfenbaum and others, 2015).

One of the largest dam removal projects occurred on the Elwha River between 2011 and 2014 (Warrick and others, 2009), when the Elwha and Glines Canyon Dams were removed. The dams were built in 1912 and 1927 and were 32 m and 64 m tall, respectively, which disrupted the natural flow of the Elwha River and halted the passage of fish and sediment. More than 90 percent of the watershed was captured by these dams, which altered downstream habitats and ecosystems (Warrick and others, 2009). Within 2 years of the dams' removal, more than 2.5 million cubic meters of sediment were deposited immediately offshore of the river mouth (Gelfenbaum and others, 2015). During the first 5 years following their removal, nearly 20 million metric tons (Mt) of sediment were eroded into the river and transported downstream, and 90 percent of this sediment (18 Mt) reached the coast (Ritchie and others, 2018). During the same 5-year period, the delta area grew by approximately 60 hectares, shifting the coastal area from a region of erosion to deposition (Ritchie and others, 2018; Warrick and others, 2019).

In situ data were collected along beach transects of the Elwha River delta beach via GNSS surveys between February 3, 2009, and November 27, 2023 (Stevens and others, 2017; Miller, 2025). From these survey data, 249 shorelines were used for comparison with SDS. Details are listed in section 4.0.

3.4. Madeira Beach

Madeira Beach, located on Florida's west coast on the 22.3 km long Sand Key barrier island in Pinellas County (fig. 5), is comprised of quartz sand beaches backed by low dunes. Structures and seawalls extend seaward of the dune in some areas. Long-term (approximately 150 years) MHW shoreline trends derived from lidar, historical maps, and imagery that incorporate the proxy-datum bias show a slight erosional trend (−0.3 meters per year [m/yr], ±0.65); whereas short-term (approximately 30 years) trends are slightly accretional (0.3 m/yr, ±0.21; Kratzmann, 2022).

Madeira Beach is an example of a highly managed beach. In 1957, the City of Madeira Beach built 37 timber and concrete groins to slow erosion. In 1961, the city built a terminal jetty and placed approximately 30,000 cubic yards of fill north of the jetty. Continued beach nourishment on a 10-year cycle since the late 1980s has further influenced and complicated the interpretation of shoreline trends.

The area experiences semidiurnal microtides with a range of 7 to 80 cm. Coastal morphodynamics are storm-dominated, mainly from tropical cyclones in the summer and fall (June through November), but also winter storms. Otherwise, the shore is dominated by small waves for most of the year, and alongshore transport is predominantly southward.

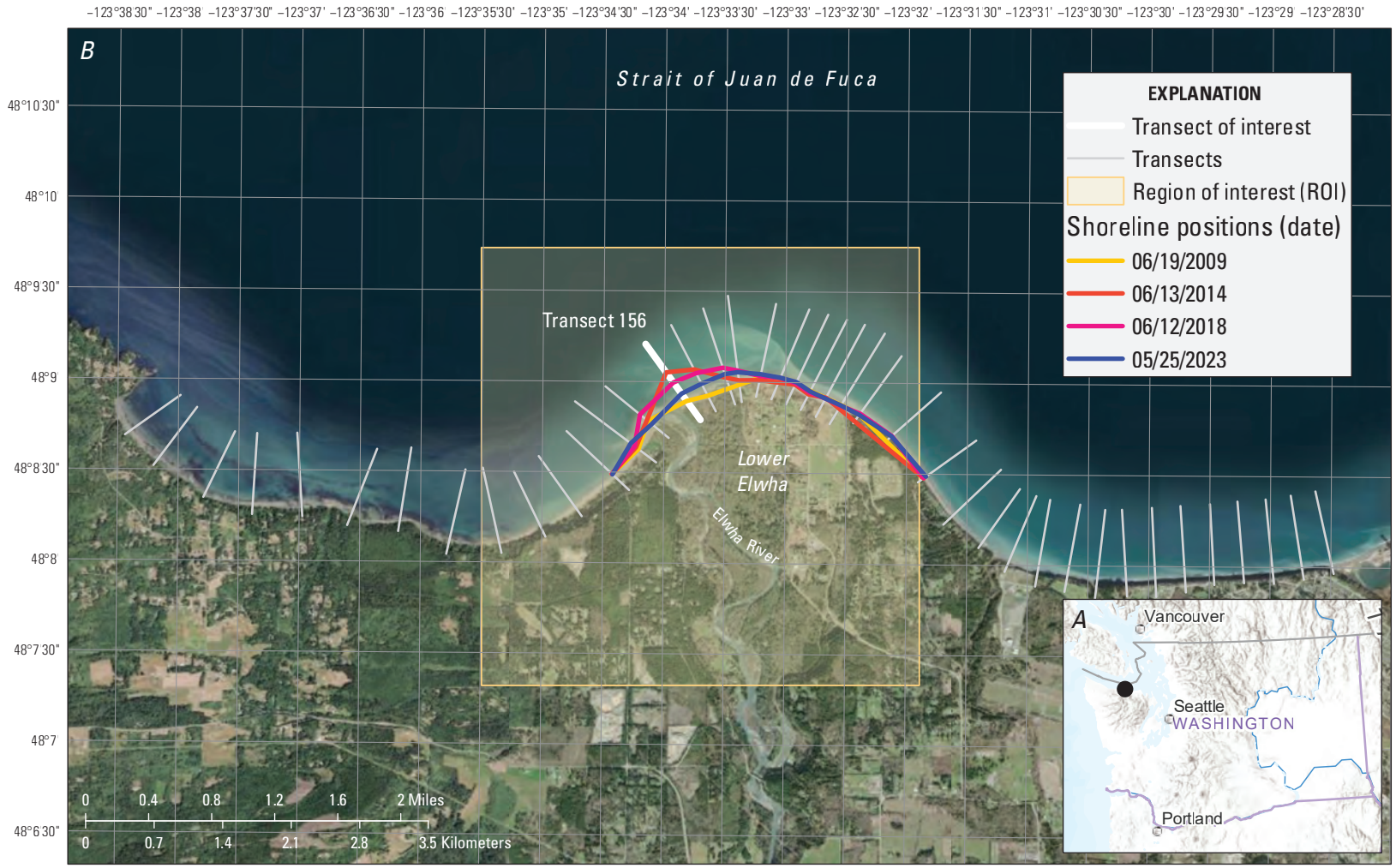

Shoreline positions from Miller (2019, 2025)
Base for all maps from Esri and its licenses, copyright 2025
Universal Transverse Mercator, zone 10 north
North American Datum of 1983

Figure 4. Historical shoreline positions for the Elwha River delta, Washington, 2009–23: *A*, study area location, and *B*, site view with the region of interest (ROI), transects, and representative traditionally sourced in situ shorelines.

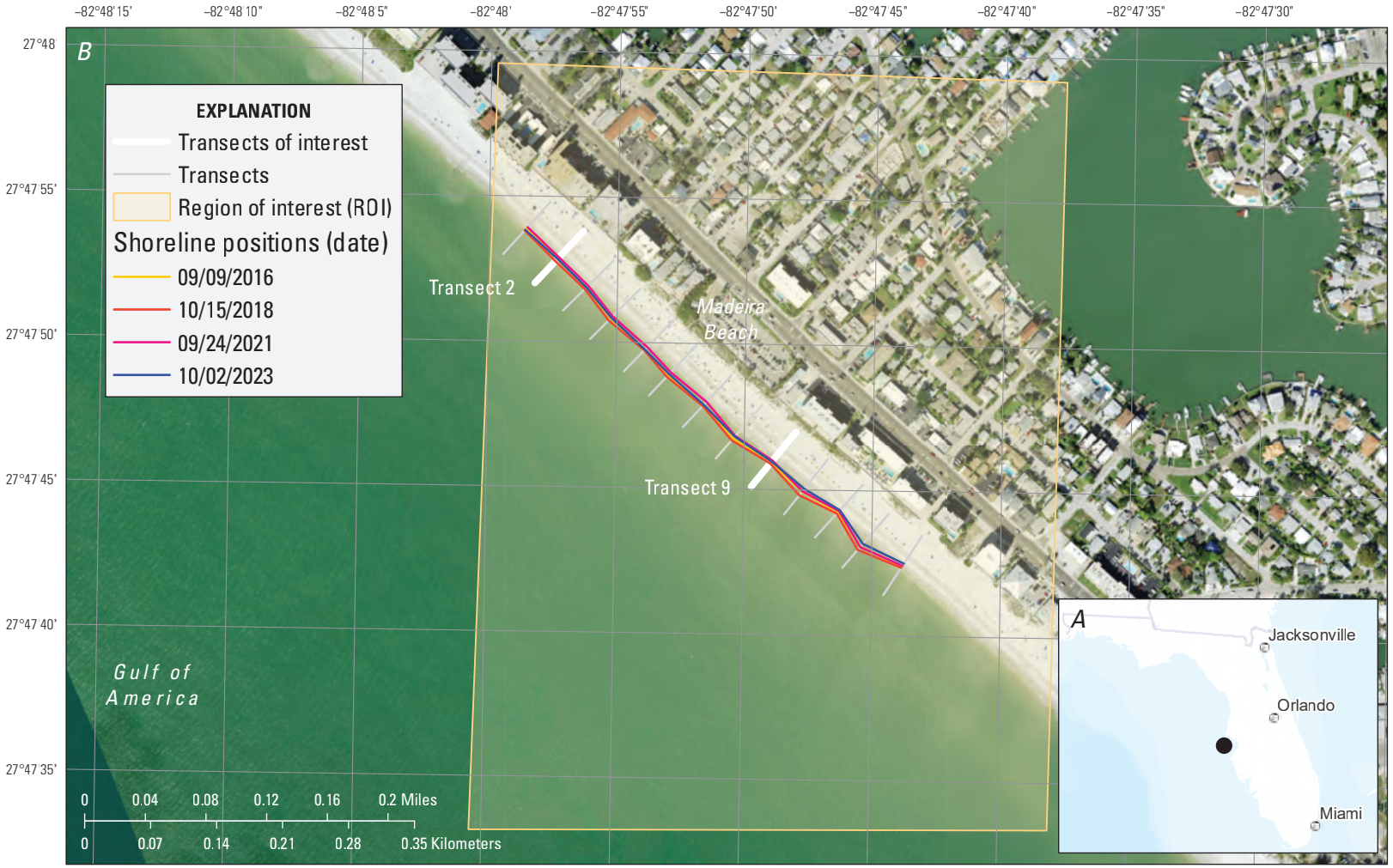

Shoreline positions from Brown and others (2018)
Base for all maps from Esri and its licenses, copyright 2025
Universal Transverse Mercator, zone 17 north
North American Datum of 1983

Figure 5. Historical shoreline positions for Madeira Beach, Florida, 2016–23: *A*, study area location, and *B*, site view with regions of interest (ROI), transects, and representative traditionally sourced in situ shorelines.

In situ data were collected for Brown and others (2018) by walking a set of beach profiles equipped with a GPS receiver and a GPS antenna affixed to a surveying backpack between 2016 and 2023. The walking surveys are used primarily to calibrate the USGS CoastCam at Madeira Beach but extend below MHW and can be used as in situ shorelines (Brown and others, 2018). There are 42 shorelines available for comparison with the SDS results from CoastSeg.

3.5. Rincón

Rincón (fig. 6) lies on the northwest coast of the Island of Puerto Rico, and the coast is comprised of reef-fronted stretches of beach backed by unconsolidated sediment and alluvial deposits. Beaches are generally sandy and narrow, showing varying levels of erosion (Thieler and others, 2007; Henderson and others, 2021). Littoral cells in this area are isolated, and there is little transport between them. New sediment primarily comes from nearshore reefs and alluvial deposits. Alongshore currents are generally to the south.

As noted by Thieler and others (1995), beach morphology at this location is influenced by seasonal storms' increased wave energy and rising sea levels, both of which can drive short-term changes in erosion rates. Construction of a marina facility in 1983 and changes in sand-management practices are thought to have contributed to increases in erosion rates at about the same time. Prevalence of urbanized shoreline fronted by seawalls and revetments has also increased in the region since the 1990s (Thieler and others, 1995).

In situ data were collected from topographic surveys, lidar, and manual extraction from imagery between 1901 and 2023, and compiled MHW and high-water line shorelines were processed and released in cooperation with the Coastal Research and Planning Institute of Puerto Rico (Henderson and others, 2021). Timing and temporal density of the in situ data do not resolve shoreline changes associated with individual wave or storm events (Thieler and others, 2007), and recent in situ data are very sparse. Only two shorelines are used from the survey data as a comparison with the new SDS results from CoastSeg because of insufficient time overlap with the SDS (refer to section 4.0 for more details). However, the Rincón site is included because many coastal study locations and communities across the United States also lack sufficient spatial and temporal data needed to evaluate changes in shoreline positions.

4.0. Methods

We used the CoastSat workflow re-implementation within CoastSeg (ver. 1.2; Fitzpatrick and others, 2024a), or CoastSeg:CoastSat, to identify and extract shorelines from all available Landsat 5 (L5), Landsat 7 (L7), Landsat 8 (L8), and Landsat 9 (L9) satellite imagery (U.S. Geological Survey, 2020a, b, c) for each site during their respective observation records (table 1). For Barter Island, Sentinel-2 imagery (European Space Agency, 2017) was also used. Version 1.2 of CoastSeg leverages CoastSat functions and workflow, and output is saved in several formats, including shoreline positions in Geographical JavaScript Object Notation (GeoJSON) format (points and vectors; Butler and others, 2016) with a high spatial density and comma-separated-values (CSV) text files. We used the output CSV files representing the location of the shoreline on prescribed transects (table 2) to do quantitative comparisons to in situ MSL or MHW shorelines at each site.

The CoastSat workflow (Vos and others, 2019b) uses Landsat and Sentinel-2 imagery to map the instantaneous waterline position from top-of-atmosphere multispectral imagery. Blue, green, red, near-infrared (NIR), and shortwave-infrared (SWIR1) bands, which were downloaded using the Google Earth Engine's (Gorelick and others, 2017) Application Programming Interface, are used for shoreline identification. L7 Enhanced Thematic Mapper Plus green, red, and NIR bands are pansharpened, whereas the blue and SWIR1 bands are up-sampled from a 30 m to a 15 m spatial footprint. Likewise, L8 and L9 Operational Land Imager blue, green, and red bands are pansharpened, and the NIR and SWIR1 bands are up-sampled from a 30 m to 15 m spatial footprint. L5 Thematic Mapper bands do not include a panchromatic band, so they are up-sampled from 30 to 15 meters per pixel (m/px) using bilinear-interpolation. Sentinel-2 Multispectral Imager blue, green, red, and NIR bands have a native spatial footprint of 10 m, and the SWIR1 is up-sampled from 20 to 10 m/px. To map the position of the sand-water interface, an ML image classifier is applied to the image to label the "sand" and "water" pixels. If sand and water pixels are detected, the Otsu thresholding technique (Otsu, 1979) is used to differentiate sand and water based on pixel values of the Modified Normalized Difference Water-Index (MNDWI; Xu, 2006). If the ML classifier fails to detect adjacent sand and water pixels, a fallback method is employed, using a value of 0.5 to differentiate land and water in the MNDWI spectral index.

Shorelines were extracted using several variations of factors that can be controlled or set within CoastSeg:CoastSat. These variations, or experiments, allowed for the investigation of how water level correction and slope may influence results across a large region encompassing a range of water levels and foreshore slopes; refer to sections 4.1 through 4.5 and table 2. Corrections for tidal water levels at the time of image acquisition are recognized as an important step in the SDS workflow for improving SDS accuracy (Vitousek and others, 2023a, b). The influence of slope is less understood, particularly in areas with complex morphologies. Wave setup also may have a significant impact on positional accuracy for individual shorelines at wave-dominated sites (Vitousek and others, 2024), but application of a setup correction does not

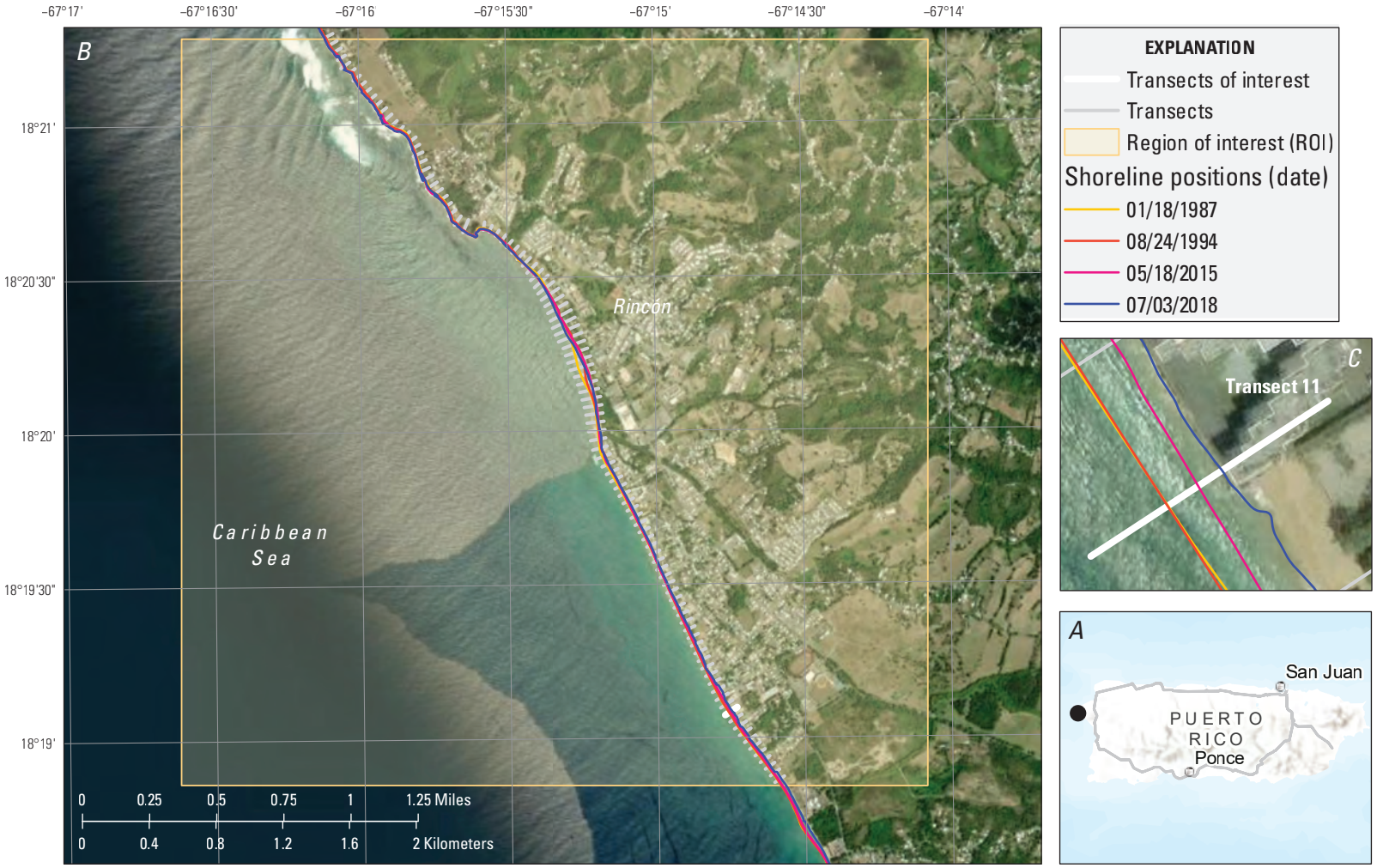

Shoreline positions from Henderson and others (2021)
Base for all maps from Esri and its licenses, copyright 2025
Universal Transverse Mercator, zone 19 north
North American Datum of 1983

Figure 6. Historical shoreline positions for Rincón, Puerto Rico, 1989–2018: *A*, study area location; *B*, site view with regions of interest (ROI), transects, and representative traditionally sourced in situ shorelines; and *C*, detailed view of transect 11.

Table 2. CoastSat workflow re-implementation within CoastSeg (CoastSeg:CoastSat) settings used for each location and for different experiments to quantify the effects of tidal correction and scalar beach slope: no tidal correction, high-slope correction, low-slope correction, and average-slope correction.

[More detailed information on settings is in Buscombe and Fitzpatrick (2023) and Fitzpatrick and others (2024a, b). All settings and data are from Buscombe and others (2025). km², square kilometer; m, meter; NA, not applicable; m², square meter; MSL, mean sea level; MHW, mean high water; ROI, region of interest]

Location	ROI size (km²)	Transect			Reference shoreline		Cloud mask		Minimum shoreline length (m)	Minimum beach area (m²)	Tidal correction datum[4]	Slope values used		
		Type[1]	Spacing (m)	Length (m)	Type[1]	Buffer distance[2] (m)	True or false	Distance[3] (m)				Low	High	Average
Barter Island	20	Custom	50	1,000	Custom	1,000	False	NA	50	50	MSL	0.01	0.15	0.07
Cape Cod	20	Custom	50	350–380	Default	70	True	20	300	6,750	MHW	0.061	0.201	0.131
Elwha River delta	20	Custom	140–500	700–1,000	Custom	320	False	NA	150	150	MHW	0.1	0.15	0.125
Madeira Beach	0.5	Custom	35–50	75	Default	100	True	300	500	1,000	MHW	0.033	0.1596	0.080
Rincón	20	Custom	30–100	33–153	Default	100	False	NA	500	1,000	MSL	0.0211	0.3968	0.1287

[1]Type is either the default available in CoastSeg:CoastSat or created in separate software and uploaded (custom).

[2]Buffer defines the distance around the reference shoreline that limited extraction of SDS.

[3]If cloud masking was used (true), a minimum distance was specified from cloud areas to begin extraction and avoid false detections.

[4]The vertical reference of in situ data used in comparisons. SDS data were tidally corrected to the reference elevation.

always improve SDS accuracy (Vos and others, 2023), and accounting for that was beyond the objectives and technical bounds of this study.

Four experiments were conducted to quantify the effects of tidal correction (using the FES2014 model) and a scalar slope on the extracted shoreline position for the five test sites (Lyard and others, 2021). In addition to a "no tidal correction" experiment, three different slope values (high, low, and average) were used to tidally correct shorelines to a consistent elevation, to show potential impacts of spatial or temporal slope variation in corrections, or to simulate the uncertainty because of misspecification of slope in locations with limited survey data.

For Cape Cod, the Elwha River delta, and Madeira Beach, slope values were determined from in situ beach survey data (Stevens and others, 2017; Brown and others, 2018; Farris and others, 2020). Average slope values were derived as the mean value from the respective datasets used in this analysis, and high and low slope values were defined as ±2 standard deviations away from the mean.

Because detailed slope data were not available for Barter Island, slopes at Barter Island were determined empirically from various locations across the site based on elevation data from 2014 to 2015 (Gibbs and others, 2019a). High, low, and average slope values were derived from the aggregate data. For Rincón, slope values were similarly determined across the study area based on a single, separate elevation dataset from 2018 (Doran and others, 2017).

CoastSeg:CoastSat accepted GeoJSON files of custom transects (landward points of origin), reference shorelines, and regions of interest (ROIs) for sites, if default features or data within CoastSeg:CoastSat were not used (table 2). Custom transects were generated for all sites using the Digital Shoreline Analysis System (DSAS; Himmelstoss and others, 2021) at a horizontal spacing of 50–100 m, with exception of the Elwha River delta where larger transect spacings were 140–500 m to coincide with in situ survey transects but with correct orientation for CoastSeg; transect identification numbers were then adjusted to depict consecutive numbering alongshore across each site.

Each site presented different challenges regarding setup for SDS extraction. Settings, details, and the unique considerations for SDS extraction follow for each site and are listed in table 2. Three principal settings were adjusted to find optimal values: the distance to a cloud pixel, minimum shoreline length in meters, and minimum beach area in square meters. These represent controls from the original CoastSat methodology (Vos and others, 2019b) used to ensure quality data. In addition to this original CoastSat implementation, we opted to filter outliers from the resulting timeseries on individual transects in our CoastSeg:CoastSat implementation. This was achieved using a recursive Hampel filter (Liu and others, 2004) with a window length of three observations and two median absolute deviations. In other words, if a cross-shore position within a length of three observations differs from the median by more than two median absolute deviations, it is dropped. This filter is applied recursively until no additional points can be removed. This was followed by dropping points above the 75th percentile of daily shoreline change. Previous studies have also used a variety of techniques for SDS data post-processing and smoothing ahead of comparison with in situ shorelines. For example, Almeida and others (2021) smoothed extracted shorelines using a one-dimensional Gaussian filter, and Castelle and others (2021) discarded shorelines below a tidal elevation of 0.2 MSL because the complex intertidal zone waterlines were not a good proxy of the shoreline position.

4.1. Barter Island

Custom ROIs were created for Barter Island to better capture the complex morphology and preserve ocean and land proportions in imagery (fig. 2; Vos and others, 2019b); ROIs were sized to be the same default areas created in CoastSeg (20 km^2). A custom shoreline based on the 2020 in situ shoreline was created and used as the reference shoreline. DSAS was used to cast custom transects at 50 m intervals, and transects were made to be very long (up to 1,000 m) to accommodate the large changes over the historical comparison period. Because of the challenging environment and complicating factors in imagery (dynamic change, weather, narrow beaches), a maximum buffer distance (1,000 m) and minimum length or area values (50 m, 50 square meters) were used to extract data; more restrictive buffers greatly reduced the ability of the system to identify shorelines, especially in areas with the largest shoreline change such as around bluffs, at the ends of spits, and where barrier islands narrowed. Cloud masking was not used because there was a problem with the masking algorithm conducted on the collected imagery in this location. All available imagery for the typically ice-free months of June through October was downloaded (see section 4.0) and reviewed, and "bad" imagery (degraded by the presence of clouds, ice, or affected by other sensor problems) was removed manually. The CoastSeg:CoastSat shoreline detection process was run, images with bad detections were additionally removed, and the shoreline detection process-step was repeated again. Approximately 1,400 images remained (173 from L5, 460 from L7, 351 from L8, 73 from L9, and 369 from Sentinel-2). In situ data used in this comparison were referenced to MSL, and all SDS data were tidally corrected to MSL (table 2).

Transects 154–206, which cover an extremely dynamic area at the end of Bernard Spit and eastern Barter Island, were removed from quantitative analysis because of excessive noise. This area is addressed separately in section 5.0.

4.2. Cape Cod

ROIs were generated within CoastSeg:CoastSat (at default 20 km^2) for all of the Cape Cod National Seashore. Three consecutive ROIs along the central portion of the

outer Cape were selected for this experiment, spanning a total of 9.5 km along the coastline (fig. 3). Satellite imagery download and shoreline extraction were performed on each ROI independently. The default CoastSeg:CoastSat reference shoreline was used, and DSAS was used to cast custom transects at 50 m intervals. After downloading all available satellite imagery from May 1984 through July 2023 for all ROIs (2,170 images total) using cloud masking, the images were manually inspected to determine their quality for shoreline extraction. Images of poor quality caused by clouds, sensor problems, and other image issues were removed (moved from usable imagery to "bad" imagery), leaving 1,735 images (80 percent) for shoreline extraction. The shoreline detection process-step was performed, results were visually inspected, and erroneous shoreline detections were removed. A total of 1,589 shorelines remained for analysis (640 from L5, 646 from L7, 248 from L8, and 35 from L9). In situ data used in this comparison were referenced to MHW, and all SDS data were tidally corrected to MHW (table 2). Unique challenges presented by bad shoreline detections are addressed separately in section 5.0.

4.3. Elwha River Delta

An ROI was generated within CoastSeg around the mouth of the Elwha River to capture shoreline evolution, but a custom shoreline was used as the reference to help capture the dynamic changes over the comparison period. Custom transects used in surveys (Miller, 2025) were adjusted for correct orientation. Removal of dams on the Elwha River by 2014 allowed for considerable growth of the river mouth delta; therefore, the reference buffer was increased to be large enough to allow for hundreds of meters of changes to the shoreline driven by the increases in sediment delivery. However, buffers set at maximum settings resulted in erroneously identified small sand bars, so the buffer was set at 320 m to capture significant shoreline changes and avoid erroneous detections. The default CoastSeg:CoastSat sand-color setting (Fitzpatrick and others, 2024a) was used at the Elwha River delta, even though the delta contains grey sand and sediment. The dark sand option in CoastSeg:CoastSat led to much poorer outputs than the default setting. Clouds, haze, and even dark-colored water were incorrectly identified by the classifier as sand with the dark-sand setting, yielding poor shoreline results.

After downloading the imagery, initial detections were reviewed, imagery with bad detections caused by clouds, weather, or other image issues was manually removed, and the shoreline detection process was rerun. Approximately 1,260 images remained (522 from L5, 451 from L7, 232 from L8, and 55 from L9). Given original survey data and complex beach profiles at the site, in situ data used in this comparison were referenced to MHW, and all SDS data were tidally corrected to MHW (table 2).

4.4. Madeira Beach

One ROI of 0.5 km^2 was generated for Madeira Beach within CoastSeg:CoastSat to cover the 500 m alongshore extent of the in situ shorelines. The default CoastSeg:CoastSat reference shoreline was used, and transects were cast at 50 m intervals to align with the in situ transects. Defaults for reference buffer distance, minimum shoreline length, and minimum shoreline area were used.

After downloading imagery, initial detections were reviewed and imagery with bad detections because of clouds, weather, or other image issues was manually removed, and the shoreline detection process was rerun. Approximately 110 images remained (0 from L5, 38 from L7, 58 from L8, and 13 from L9). In situ data used in this comparison were referenced to MHW, and all SDS data were tidally corrected to MHW (table 2).

4.5. Rincón

An ROI of 20 km^2 was generated for Rincón within CoastSeg:CoastSat for the area, and the default reference shoreline was used. Transects from in situ shoreline records (Henderson and others, 2021) were used in CoastSeg:CoastSat after adjusting for correct orientation. Defaults for reference buffer distance, minimum shoreline length, and minimum shoreline area were used. Cloud masking was not used because there were complications with masks in this area, and cloud cover was a significant challenge. All imagery for the comparison period was downloaded and reviewed, and bad images were removed manually. Initial shoreline detection images were reviewed, and images with bad detections were additionally removed; the shoreline detection process-step was then repeated. Approximately 150 of the images remained (5 from L5, 17 from L7, 104 from L8, and 19 from L9). In situ data used in this comparison were referenced to MSL, and all SDS data were tidally corrected to MSL (table 2).

There was a clear offset between SDS and in situ observations during the earlier portion of the comparison period (prior to 2012) because in situ shorelines prior to 2012 were derived from wet-dry line in imagery without appropriate proxy-datum bias corrections; however, correcting this offset was beyond the scope of this effort. Additionally, the beaches were narrow during this period and more difficult for manual identification in lower resolution imagery. Therefore, statistical comparisons are limited to the data after 2012, leaving only two in situ shorelines.

4.6. Techniques for Data Analysis

SDS measurements were compared with in situ shoreline data for each location (Barter Island, Cape Cod, the Elwha River delta, Madeira Beach, and Rincón) and for each experiment (no tidal corrections, low slope corrections, average slope corrections, and high slope corrections). For this analysis, all SDS observations within 10 days of an in situ measurement were considered. The resulting timeseries of comparison SDS at all transects was filtered using a Hampel filter to remove outliers. Additionally, points that were above the 75th percentile of daily shoreline change were also removed in Barter Island and the Elwha River delta. Errors between each SDS–in-situ pair across all transects were computed, and then the mean error (ME; eq. 1), mean absolute error (MAE; eq. 2), root mean squared error (RMSE; eq. 3), mean absolute percentage error (MAPE; eq. 4), and root mean squared percentage error (RMSPE; eq. 5) were computed from the distribution of errors using the following:

$$ME = \frac{\sum_{i=1}^{n} x_{in-situ,\,i} - x_{SDS,\,i}}{n}, \tag{1}$$

$$MAE = \frac{\sum_{i=1}^{n} \left| x_{in-situ,\,i} - x_{SDS,\,i} \right|}{n}, \tag{2}$$

$$RMSE = \sqrt{\frac{\sum_{i=1}^{n} \left(x_{in-situ,\,i} - x_{SDS,\,i} \right)^2}{n}}, \tag{3}$$

$$MAPE = \frac{\sum_{i=1}^{n} \left| \left(\frac{\left(x_{in-situ,\,i} - x_{SDS,\,i} \right)}{x_{in-situ,\,i}} \right) \right| \times 100}{n}, \quad \text{and} \tag{4}$$

$$RMSPE = \sqrt{\frac{\sum_{i=1}^{n} \left(\frac{\left(x_{in-situ,\,i} - x_{SDS,\,i} \right)}{x_{in-situ,\,i}} \right)^2 \times 100}{n}}, \tag{5}$$

where

n is the number of observations,
$x_{in-situ}$ is the in situ cross-shore position, and
x_{SDS} is the SDS cross-shore position.

These results are depicted in figures for each site in section 5.0. Each figure shows the ME, MAE, MAPE, RMSE, and RMSPE, the interquartile range (IQR) of SDS observations, and the number of observation pairs at all transects noted. A variety of metrics are presented to illustrate different properties of the shoreline measurements. MAE and RMSE provide a single number for each experiment, estimating the magnitude of error (or deviation between SDS and more traditional techniques); RMSE is more sensitive to outliers, whereas ME is indicative of bias. MAPE and RMSPE further contextualize the error for each site relative to the amplitude of the signal present in each set of shoreline position timeseries. Like RMSE, RMSPE is more sensitive to outliers. MAPE and RMSPE allow for normalized comparisons between sites that show vastly different magnitudes of shoreline change. The IQR, an estimate of signal variance based on the difference between the 25th and 75th percentiles, contextualizes the MAE and RMSE estimates. For example, if the computed error metric (either RMSE or MAE) is nearly equal to the IQR for a given site, then the signal measured is likely mostly noise. However, if the computed errors have much smaller values compared to the IQR, then there is more evidence that the shoreline measurements have captured a true signal. To support the results shown in those figures, timeseries of SDS for select transects of interest (figs. 2, 3, 4, 5, 6) are also shown for each site, along with the range of SDS values and the SDS mean value from all four experiments; in situ data not used in the comparisons are also plotted for additional context. Additionally, MAE and RMSE were computed for each transect, and the per-transect MAE (from the experiment with the lowest error values) across the study area is illustrated. Linear trends of the comparison SDS over the entire period from the same experiment are also shown.

To illustrate shoreline behavior across each site's entire observation period, outside of the relatively few comparison data and provide context for trends in the above analyses, all SDS data from the average-slope experiment (not only comparison SDS, but all SDS from the imagery record at each site) were plotted to show monthly change using the techniques outlined in Janda and others (2025). For sites with multiple ROIs (Cape Cod and Barter Island), the ROIs were combined to create a cohesive view of the entire site. Shoreline positions were resampled at a monthly timescale to help reduce noise, and a locally estimated scatterplot smoothing (LOESS) filter was applied to highlight monthly trends (Janda and others, 2025). Unfiltered data are also plotted, because the LOESS filter can smooth out small events. These figures are oriented in the same cardinal geographic directions as the site locations: east-west for Barter Island, the Elwha River delta, and Madeira Beach, and north-south for Cape Cod and Rincón.

5.0. Results and Comparisons of Shoreline Positions

5.1. Shoreline Trends

Differences in sampling and analysis can yield very different trend results in environmental data (Hess and others, 2001). Shoreline trends, both long-term (on the order of hundreds of years) and short-term (on the order of decades or less), are critical metrics for the coastal science community's current understanding of shoreline behavior (U.S. Army Corps of Engineers, 1984); however, previously published rates for this study's locations, as many other locations across the United States, were derived from relatively few (compared to satellite-derived data) traditionally derived shorelines. Thus, direct comparisons of trends from all SDS to existing rates are misleading. An in-depth investigation into short-term rates along select transects (figs. 2, 3, 4, 5, 6) from all study sites using only paired SDS and in situ data, showed that SDS-derived rates were comparable to traditional methods, being within the standard error of in situ rates at most transects (table 3). Across the study areas, rates from SDS were similarly comparable to rates from in situ data at 84 percent of transects at all sites except Rincón (table 4). Dynamic shoreline change, complex morphology, shadows, and excessive turbidity complicated transect-based shoreline identification and resulting comparisons at the Elwha River delta and are discussed in section 5.4. A deeper investigation into SDS–in-situ trend comparisons is presented in section 5.3.

More detailed discussions of results and comparisons follow for each study site.

5.2. Barter Island

Several challenges were encountered in extracting SDS data for Barter Island. One was the common presence of clouds and ice, and a considerable amount of time was needed to manually review imagery to filter out unusable and bad detections. The complex landscape of the barrier islands and spits and the rapidly changing shoreline also led to unique setup needs and transect orientation. For example, a particularly challenging area was at the west end of Bernard Spit, where Bernard Spit is migrating westward past the eastern Barter Island spit and Kaktovik (figs. 2, 7). The adjacency of Bernard Spit to Barter Island required special transect generation to avoid overlapping transects and spurious shoreline detection. Noisy data related to recurved finger spits associated with rapidly migrating shorelines both on

Table 3. Short-term shoreline change rates and standard error for transects of interest at all study sites, derived from in situ data and satellite-derived shorelines (SDS).

[Short-term rates are determined by linear regression at all sites except Rincón, where end-point rates are used; standard error is defined as the standard deviation of the errors for all sites except Rincón. m/yr, meters per year; NA, not applicable]

Location	Transect	In situ[1,2]		SDS[1,3]		Number of observations[1]
		Short-term rate (m/yr)	Standard error	Short-term rate (m/yr)	Standard error	
Barter Island	102	−4.6	0.4	−4.8	0.7	5
	342	14.7	8.5	15.1	8.2	9
Cape Cod	582	−1.1	0.6	−0.5	0.9	35
	649	−0.3	1.2	−1.1	1.6	35
Elwha River delta[4]	156, preceding sediment pulse	1.5	0.4	7.3	7.3	17
	156, during sediment pulse	253.2	24.0	228.9	31.0	15
	156, following sediment pulse	−28.0	1.2	−29.8	2.1	47
Madeira Beach	2	−0.3	0.2	0.4	0.5	14
	9	−0.6	0.2	−0.2	0.5	18
Rincón	46	−0.8	NA	−0.2	NA	2

[1]Only SDS observations and in situ data that were within a ±10-day window were considered.

[2]Data are from Stevens and others (2017), Brown and others (2018), Farris and others (2020), Gibbs and others (2020), Henderson and others (2021), and Miller (2025).

[3]Data are from Buscombe and others (2025).

[4]Multiple short-term rates are presented to describe shoreline behavior preceding, during, and following a sediment pulse from dam removal.

Table 4. Percentage of transects at which the satellite-derived shoreline short-term rate is comparable to (within the standard error of) the in situ rate.

[In situ shoreline data are from Stevens and others (2017), Brown and others (2018), Farris and others (2020), Gibbs and others (2020), Henderson and others (2021), and Miller (2025). Satellite-derived shoreline data are from Buscombe and others (2025). Multiple periods are presented for the Elwha River delta to describe shoreline behavior preceding, during, and following a sediment pulse from dam removal. %, percent; NA, not applicable]

Location	Transects with comparable shoreline change rates[1]
Barter Island	83.9%
Cape Cod	92.6%
Elwha River delta (preceding sediment pulse)	64.3%
Elwha River delta (during sediment pulse)	57.1%
Elwha River delta (following sediment pulse)	33.3%
Madeira Beach	92.3%
Rincón	NA
All sites (excluding Rincón)	**84.0%**

[1]Only SDS observations and in situ data that were within a ±10-day window were considered.

Bernard Spit and at the western end of Barter Island, where an older shoreline, back side of the spit, or wetland edge would be classified as the shoreline rather than the most seaward position. Identification issues seemed to occur often because of image problems or the presence of small clouds, ice, or a gap in the L7 imagery associated with the scan line corrector. Transects 154–206 were an extreme example of this behavior and contained significantly larger RMSE than adjacent transects (figs. 7, 8); they were removed from analysis. Some outliers throughout the study area were also due to the "compute intersections" function within underlying CoastSat functions. This function, in addition to returning occasional bad solutions, was cumbersome and slow in computation. Filtering techniques (Hampel and LOESS filters) reduced a lot of the noise to get usable trends and data.

After removing numerous bad images and faulty detections, the remaining 389 SDS from the four ROIs were combined for analysis. Of the 15 in situ shorelines, 12 were within 10 days of an SDS from 1987 to 2020. Of the four slope experiments, the no-corrections experiment resulted in the highest accuracy, with an RMSE of 29.6 m and MAE of 16.1 m, although there was little difference between all four experiments (figs. 7*A–D*). The similarities between the experiments may have been due to the microtidal conditions at Barter Island. Most errors between in situ and SDS observations were less than 40 m, and per-transect errors were spatially variable, with higher errors occurring at the ends of the barrier islands and spits (figs. 7*A–D*, 7*G*). MAE and RMSE were a small fraction of the IQR of observed SDS positions, indicating that the change signal was captured well despite the error in the measurements. This was evident where the SDS positions follow the same trends as the in situ shorelines between 1987 and 2020: at transect 102 (near the center of Bernard Spit), the shoreline showed a relatively consistent erosional trend through time, whereas transect 342 (near the western edge of the Barter Island spit) showed gradual retreat from 1987 to 2012, then rapid progradation of the shoreline by about 400 m followed by relative stability (figs. 7*E*, 7*F*). However, this did not represent 400 m accretion; instead, it showed alongshore migration of a more seaward fingerling spit. This location exemplified why using a transect-based approach to quantify shoreline change can provide an incomplete or misleading record of shoreline change, particularly on dynamic barrier coasts where a piece of land may have completely eroded, formed, or migrated into a location where no previous landform existed (Gibbs and others, 2019b).

Linear trends of comparison SDS showed primarily erosive trends across the site, except at the western edge of Barter Island and near the center of Barter Island (fig. 7), matching in situ data. Monthly shoreline positions from all SDS showed this erosional trend and distinct spots of accretion in more detail (fig. 8). However, artifacts from ROI boundaries were visible around the 11,000 m and 16,000 m marks (fig. 8); these artifacts stemmed from transect orientation because transects were not parallel to the ROI boundaries but crossed at oblique angles and thus only had imagery for portions of the transect (fig. 8).

A comparison of the SDS, in situ shorelines, and edge of bluff positions indicated shorelines, rather than bluff edges, were classified in the imagery where both were present. However, the width of the coastal bluff shadow was similar to the width of the beach, which may have contributed to the accurate identification of the shoreline.

There were several high-error outliers skewing error distributions, but these stemmed from only a few transects. These outliers were likely a mix of classifier error (erroneous shoreline detection), the shoreline contour being detected at the backside of the barrier island, an older, abandoned fingerling on a barrier spit, or a wetland feature behind a barrier spit. These latter sources of error were common with the L7 data where the "striping" or gaps in the imagery associated with the failure of the scan line corrector fell over the seaward shoreline along a transect (fig. 9).

Despite these substantial challenges in detection, even in the most challenging and high-error areas, plenty of usable data that showed shoreline evolution and behavior in sufficient detail were still extracted (fig. 9). Selected SDS for transects 154–206 showed the complex evolution of the spit end matching in situ data including the shift from accretional to erosional trends moving westward along Barter Island. However, much more time was required to clean and filter SDS data appropriately in these areas, including identifying

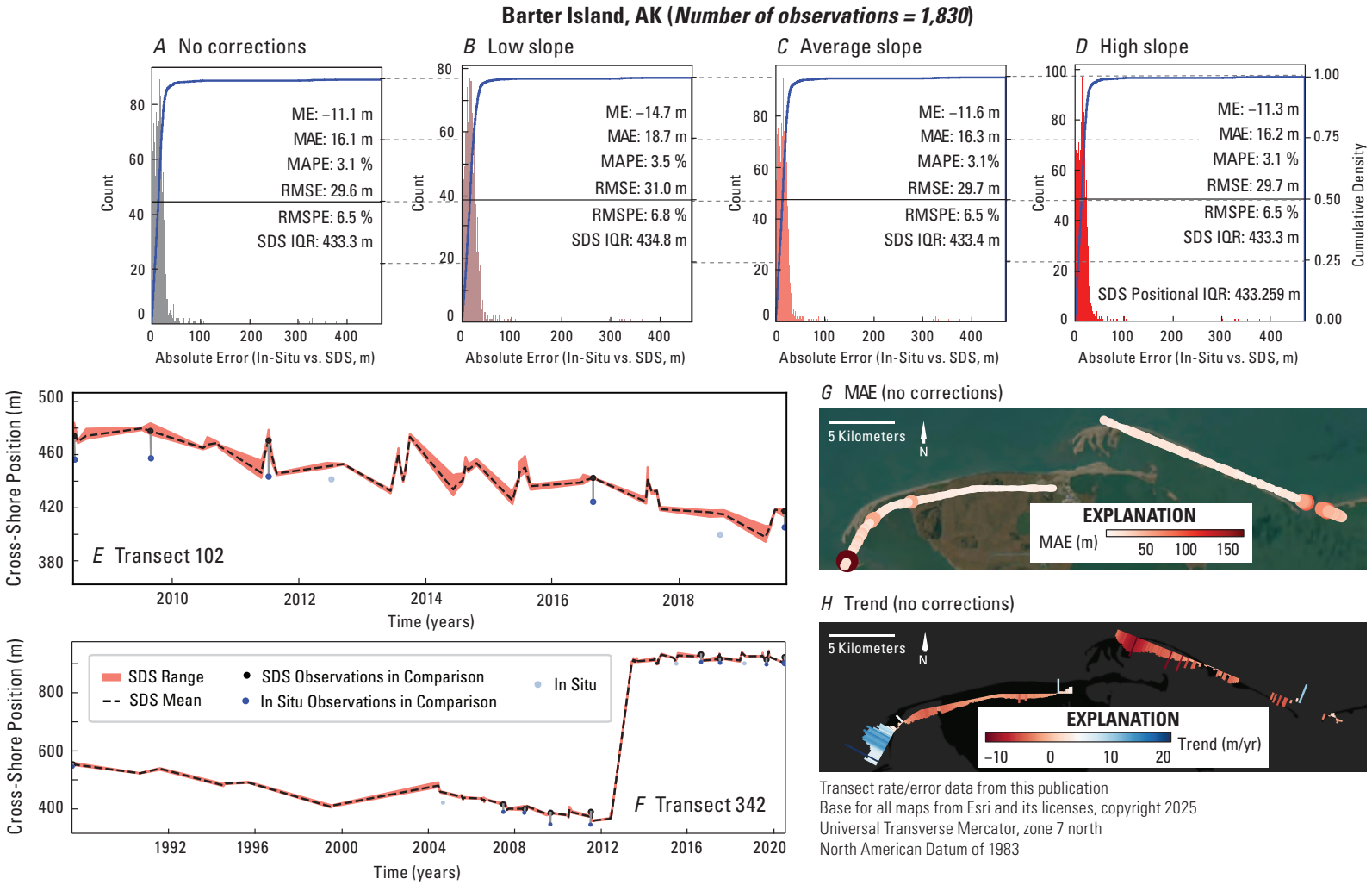

Transect rate/error data from this publication
Base for all maps from Esri and its licenses, copyright 2025
Universal Transverse Mercator, zone 7 north
North American Datum of 1983

Figure 7. Results of error analysis for Barter Island, Alaska. Plots showing the distribution of errors between in situ and satellite-derived shoreline (SDS) observations under four experiments: *A*, no tidal corrections, *B*, low slope, *C*, average slope, and *D*, high slope. Plots showing example timeseries of mean SDS positions and total range at *E*, transect 102 during 2009–19 and *F*, transect 342 during 1991–2020. Maps showing *G*, per-transect mean absolute error (MAE) and *H*, linear trends from the no-correction experiment. In situ shoreline data are from Gibbs and others (2020). Satellite-derived shoreline data are from Buscombe and others (2025). [ME, mean error; m, meter; %, percent; MAPE, mean absolute percentage error; RMSE, root mean squared error; RMSPE, root mean squared percentage error; IQR, interquartile range; vs., versus; km, kilometer; m/yr, meters per year]

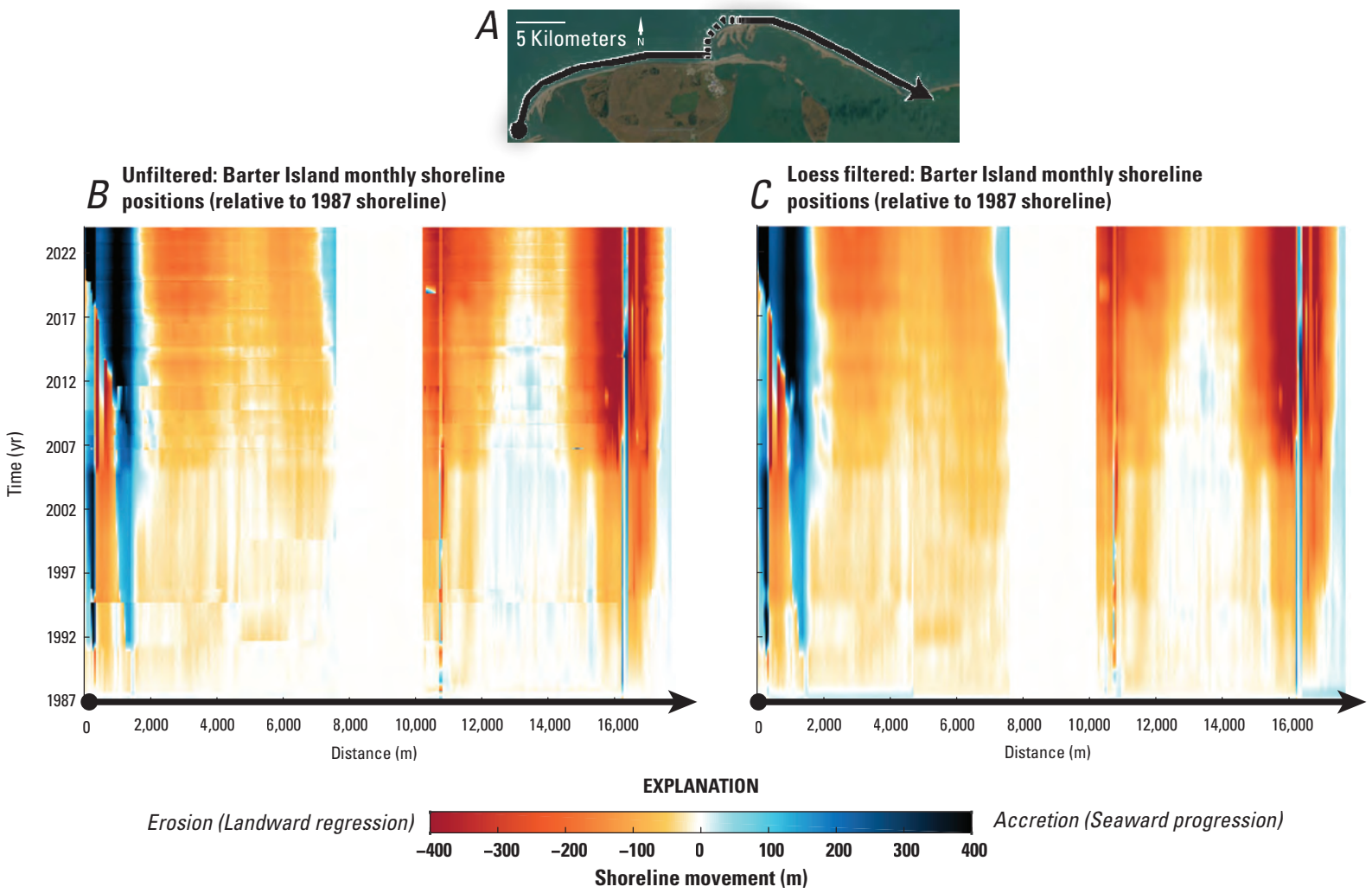

Base for all maps from Esri and its licenses, copyright 2025
Universal Transverse Mercator, zone 7 north
North American Datum on 1983

Figure 8. Monthly resampled locally estimated scatterplot smoothing (LOESS) shoreline positions for Barter Island, Alaska, 1987–2023, shown with respect to the 1987 shoreline position: *A*, study area location and orientation, *B*, shoreline positions without filter, and *C*, positions with low-pass filter. Satellite-derived shoreline data are from Buscombe and others (2025). [km, kilometer; yr, year; m, meter]

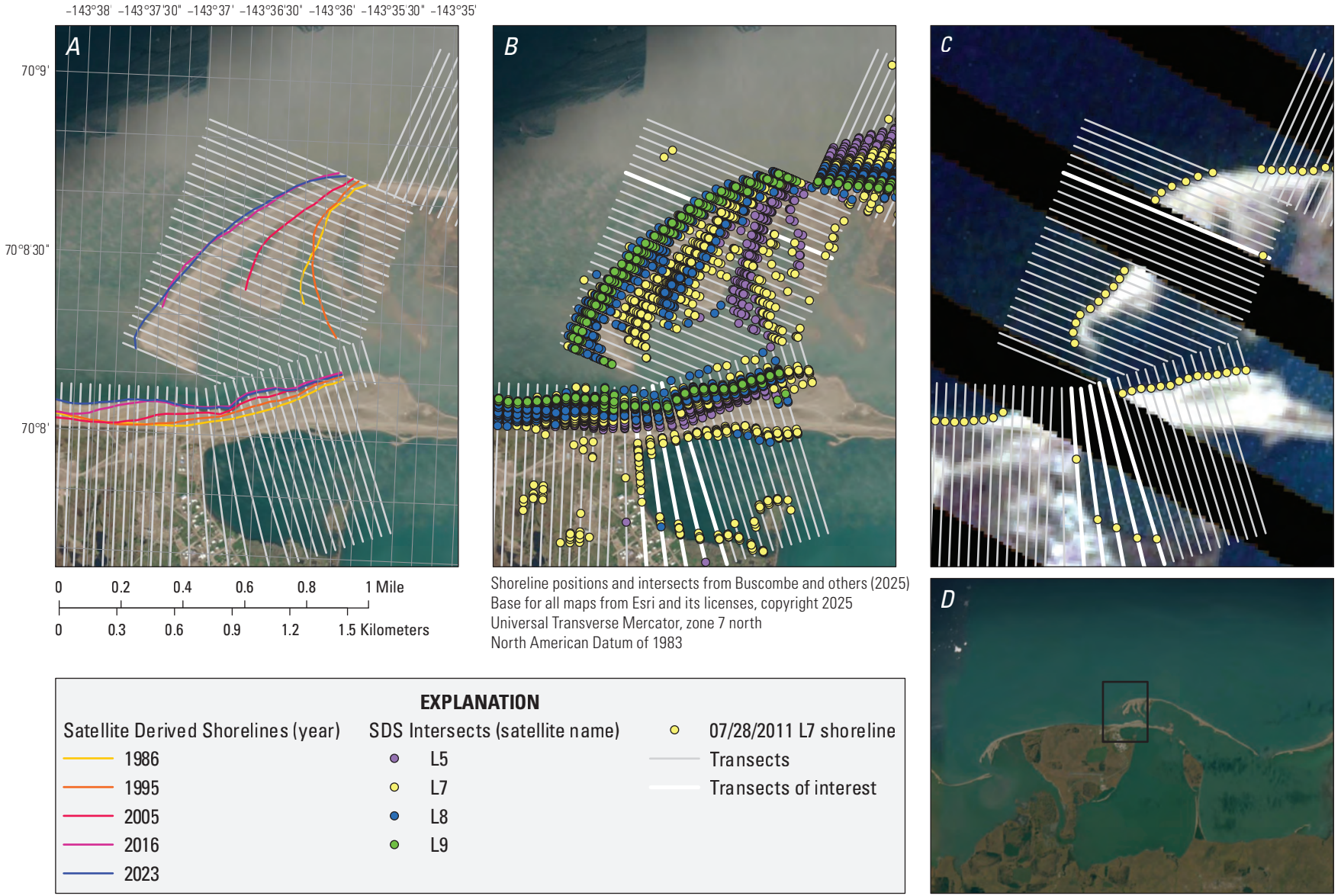

Figure 9. Maps of Barter Island, Alaska, showing satellite-derived shorelines (SDS) for transects 154–206 and pattern of shoreline evolution during the study period, 1986–2023: *A*, select SDS instances during the study period; *B*, all SDS positions captured by Landsat during the study period; *C*, transects and SDS positions for a Landsat 7 (L7) image captured on July 28, 2011, displayed over the source imagery (U.S. Geological Survey, 2020b) to illustrate striping issue common in this satellite's data; and *D*, study area location. Satellite-derived shoreline data are from Buscombe and others (2025). [L5, Landsat 5; L8, Landsat 8; L9, Landsat 9]

sources of the largest error. At this location, most of the largest errors were due to the L7 data, which included imagery gaps ("striping") that led to the misidentification of inland features as shorelines and bad shoreline identifications (fig. 9).

5.3. Cape Cod

Unique challenges related to nearshore bars and breaking waves were encountered when extracting SDS at Cape Cod. Whereas the beach at this site is often relatively straight and uncomplicated, the occurrence of welded bars, longshore bars, and occasional breaking waves unexpectedly complicated shoreline extraction at this location. The presence of these features was periodically the cause of bad shoreline detections, manifesting as gaps in the extracted shoreline, double (or triple) shorelines at the same location, and overly sinuous sections of shoreline (fig. 10). Through iterative testing to determine the optimal CoastSeg:CoastSat settings (table 2), the occurrences of these artifacts and bad shoreline detections were reduced. However, even with optimal settings selected, 8.4 percent of the shorelines were manually removed from the final dataset because of bad detections.

The remaining SDS from the three ROIs were combined for the Cape Cod analysis. There was a total of 1,589 usable SDS, 111 in situ shorelines, and 59 in situ shorelines within 10 days of an SDS between 1998 and 2005. Of the four slope experiments, the average slope resulted in the lowest error with an RMSE of 9.9 m and MAE of 7.2 m (figs. 11*A–D*). Most errors between in situ and SDS observations were less than 30 m, and per-transect errors appeared to be randomly distributed along the site (figs. 11*A–D*, 11*G*). MAE and RMSE were about one-third the IQR of observed SDS positions, indicating that the SDS effectively captured shoreline change trends comparable to in situ data on the outer Cape (figs. 11*E–F*). The SDS generally followed the same trends as the in situ shorelines between 1999 and 2002. At transect 582, the shoreline was relatively stable during this time, whereas the shoreline at transect 649 experienced tens of meters of erosion followed by approximately the same amount of accretion. After 2002, the in situ timeseries became sparser, complicating efforts to compare the trends (figs. 11*E*, 11*F*).

Overall, from 1984 to 2023, the SDS showed a primarily erosive trend interspersed with sections or bands of accretion along this section of Cape Cod National Seashore (fig. 11*H*). Monthly shoreline positions from all SDS data showed these trends of broad erosion and limited bands of accretion in more detail (fig. 12). From 1990 to 2003, there were distinct bands of erosion and accretion along the 9.5 km stretch of beach. Between 2003 and 2010, the accretional bands in the northern half of the study area began to disappear, reappearing

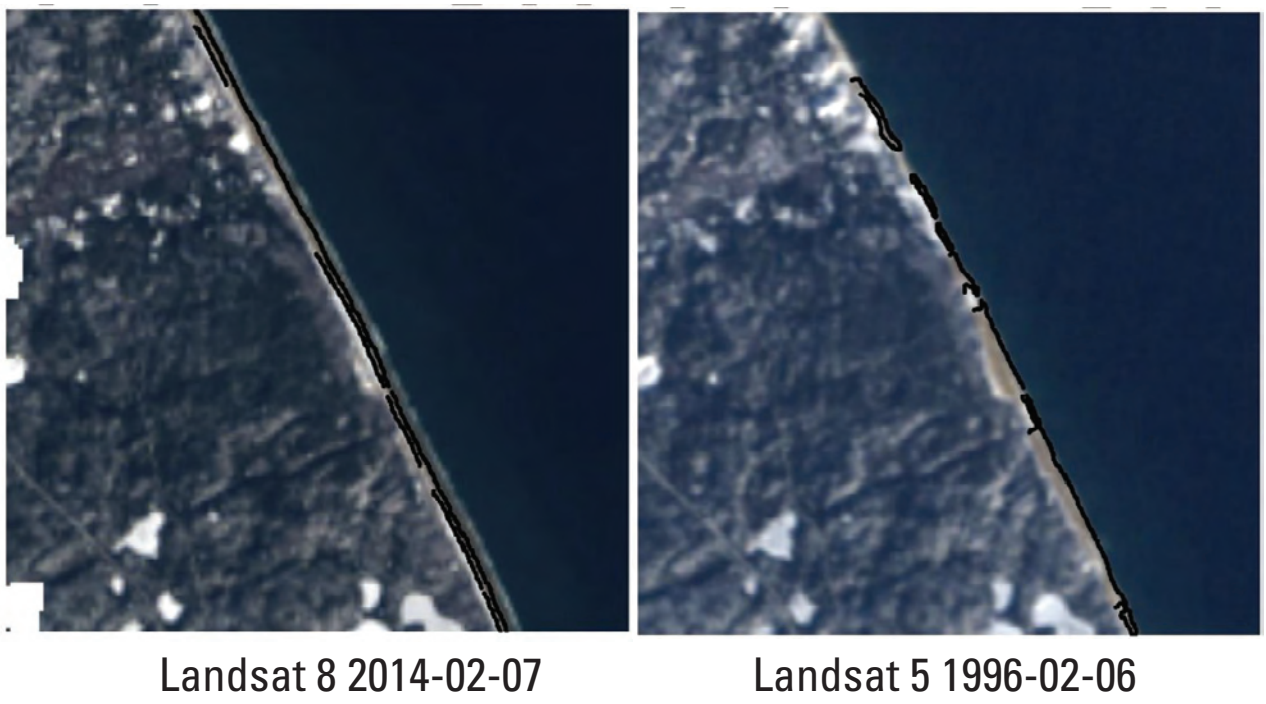

Figure 10. Examples of bad shoreline detections along a portion of the Cape Cod, Massachusetts, study area: *A*, Landsat 8 image (U.S. Geological Survey, 2020c) captured February 7, 2014, showing double shorelines, and *B*, Landsat 5 image (U.S. Geological Survey, 2020a) captured February 6, 1996, showing shoreline gaps and overly sinuous shorelines.

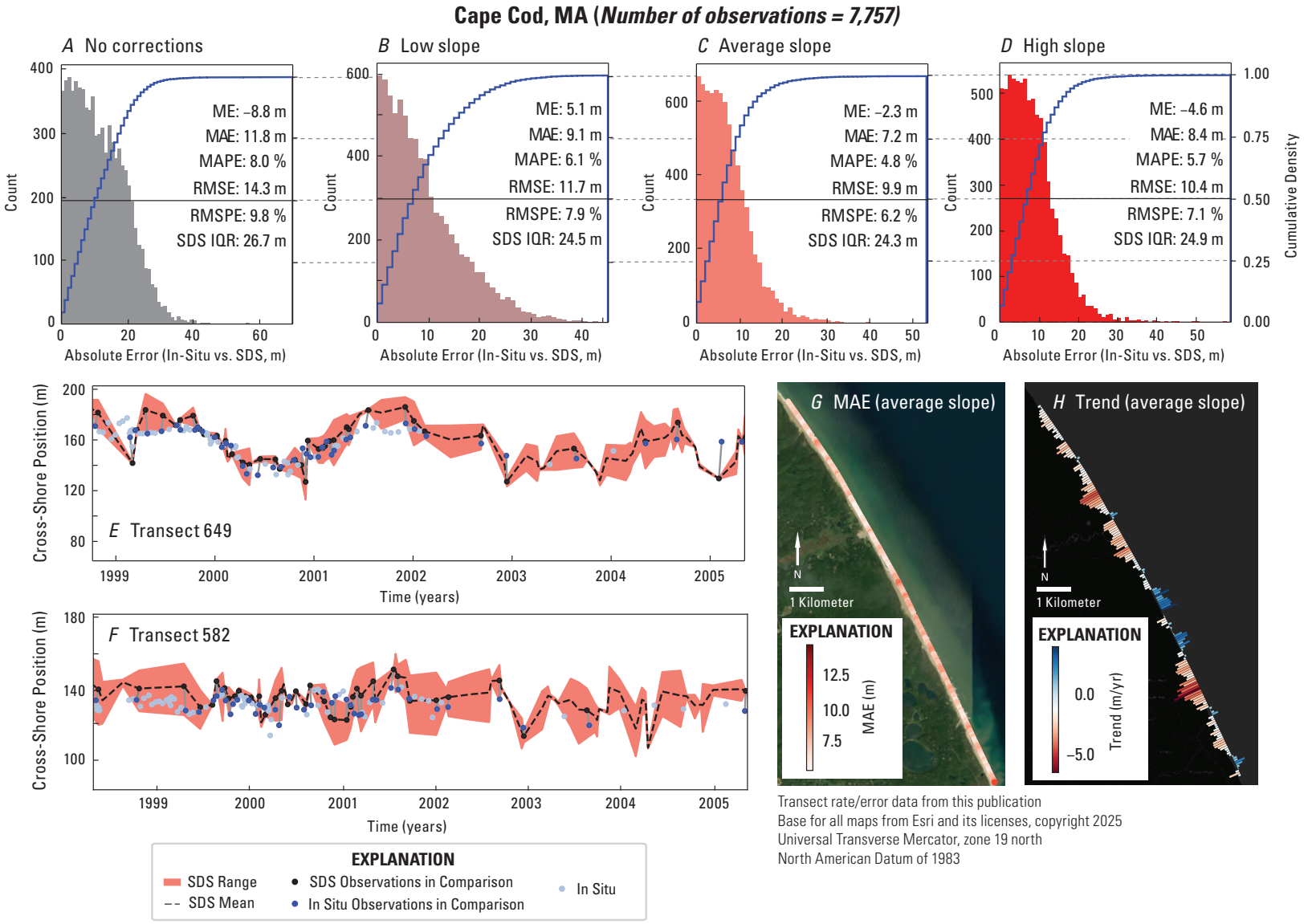

Transect rate/error data from this publication
Base for all maps from Esri and its licenses, copyright 2025
Universal Transverse Mercator, zone 19 north
North American Datum of 1983

Figure 11. Results of error analysis for Cape Cod, Massachusetts. Plots showing the distribution of errors between in situ and satellite-derived shoreline (SDS) observations under four scenarios: *A*, no tidal corrections, *B*, low slope, *C*, average slope, and *D*, high slope. Example timeseries of mean SDS positions and total range at *E*, transect 649 and *F*, transect 582 during 1998–2005. Maps showing the *G*, per-transect mean absolute error (MAE) and *H*, linear trends from an average-slope experiment. In situ shoreline data are from Farris and others (2020). Satellite-derived shoreline data are from Buscombe and others (2025). [ME, mean error; m, meter; %, percent; MAPE, mean absolute percentage error; RMSE, root mean squared error; RMSPE, root mean squared percentage error; IQR, interquartile range; vs., versus; km, kilometer; m/yr, meters per year]

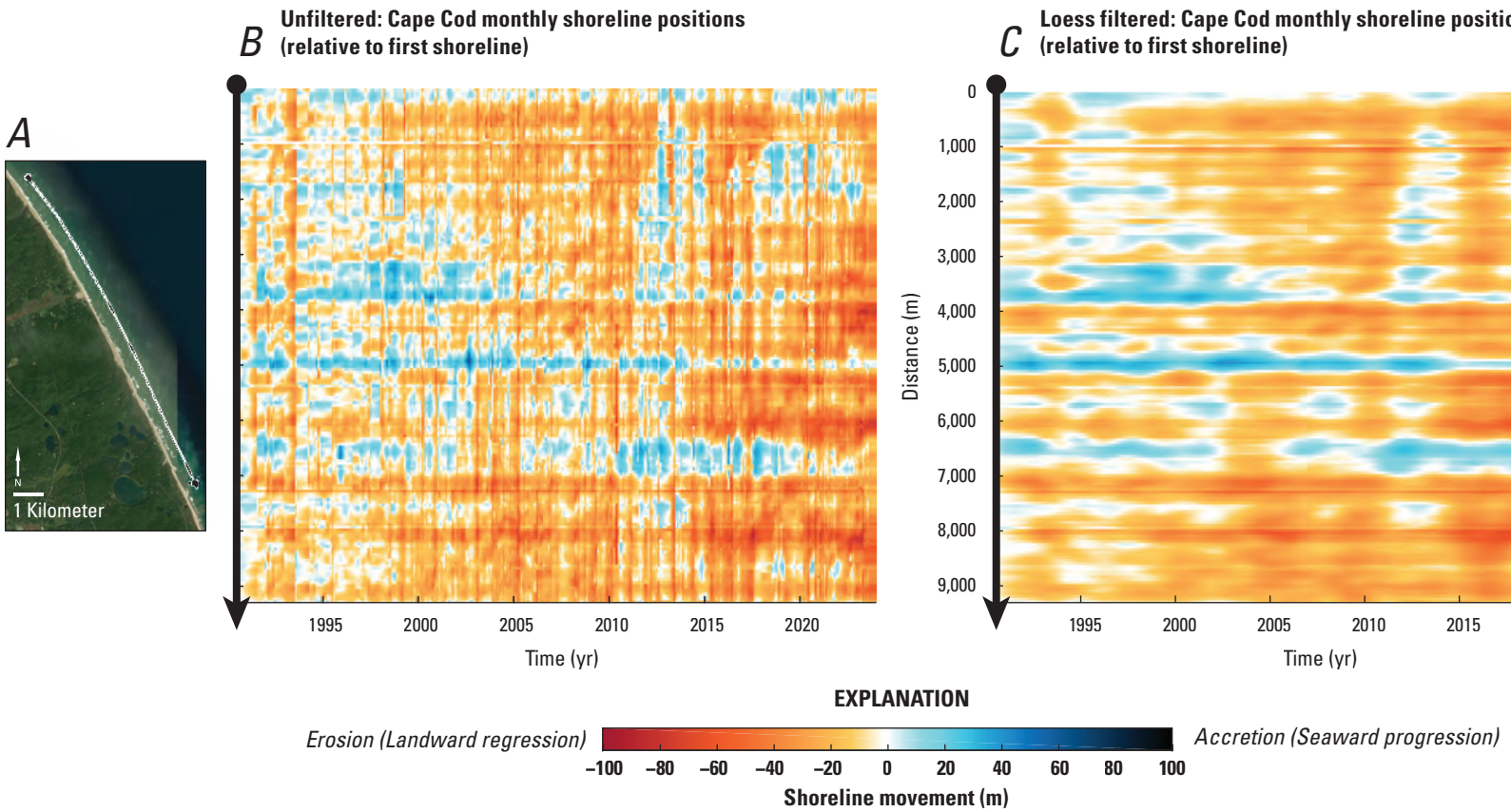

Base for all maps from Esri and its licenses, copyright 2025
Universal Transverse Mercator, zone 19 north
North American Datum of 1983

Figure 12. Monthly resampled locally estimated scatterplot smoothing (LOESS) shoreline positions for Cape Cod, Massachusetts, 1990–2023, shown with respect to the 1990 shoreline position: *A*, study location and orientation, *B*, shoreline positions without filter, and *C*, positions with low-pass filter. Satellite-derived shoreline data are from Buscombe and others (2025). [km, kilometer; m, meter; yr, year]

around 2012. By 2023, the entire study area had eroded (relative to the first shoreline) except for a very small section at 5,000 m alongshore.

Short-term shoreline change rates at this study site highlighted the importance of using appropriately matched data for trend comparisons and how differences in sampling can affect resultant trends. In this experiment, only SDS within 10 days of in situ shorelines were used for the comparisons. If there were several SDS within the ±10-day window, only the SDS closest in time to the in situ shoreline was used. When shoreline change trends (short-term change rate) using all SDS were compared to all in situ shorelines during a common time period, the trend patterns were similar over the length of the study area, showing similar spatial relationships; however, the magnitudes of change, and in some cases, the sign of the trend on individual transects differed, as shown in fig. 13. When using all SDS and all in situ data, the mean difference in trends across the study site was 1.96 m/yr (fig. 13*A*). However, when limited to only those SDS–in-situ pairs within the ±10-day window, the results improved substantially (fig. 13*B*), with the mean difference in the trends dropping by over a meter to 0.78 m/yr.

5.4. Elwha River Delta

The Elwha River delta site provided an opportunity to evaluate the skill of CoastSeg:CoastSat for SDS estimation in a mixed sediment delta undergoing rapid coastal change. After removal of bad detections, there was a total of 858 usable SDS, 249 in situ shorelines, and 138 in situ shorelines within 10 days of an SDS between 2009 and 2023. With reference to figures 14*A–D*, 50 percent of SDS measurements were within

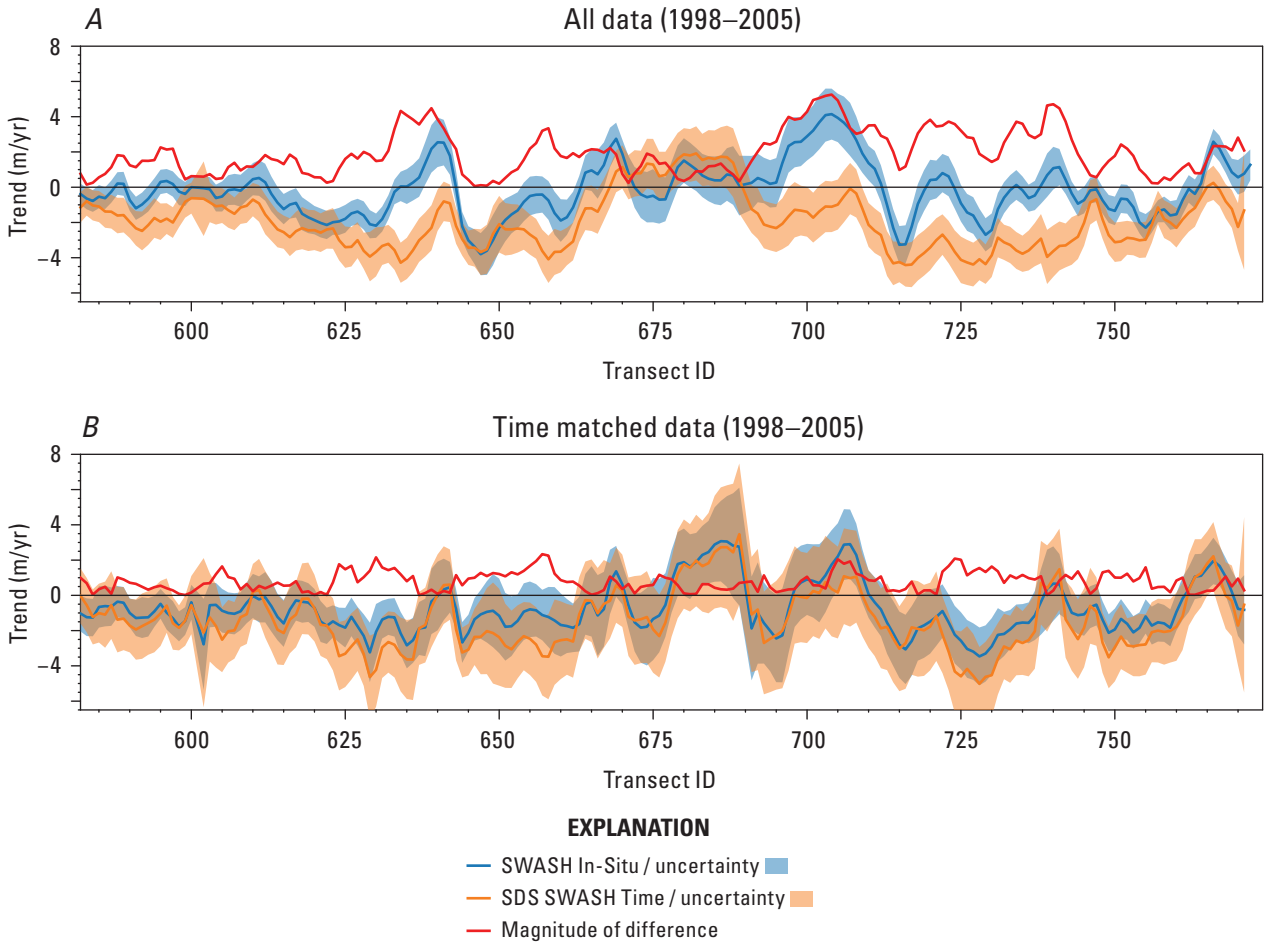

Figure 13. Plots showing per-transect linear trends, trend uncertainty, and magnitude of trend difference for satellite-derived shorelines (SDS) and in situ surveying wide-area shorelines (SWASH) of Cape Cod, Massachusetts, 1998–2005: *A*, trends and uncertainty using all available SDS and in situ data and *B*, trends only using SDS within a ±10 day window of traditionally sourced in situ shorelines. In situ shoreline data are from Farris and others (2020). Satellite-derived shoreline data are from Buscombe and others (2025). [m/yr, meters per year; ID, identification number]

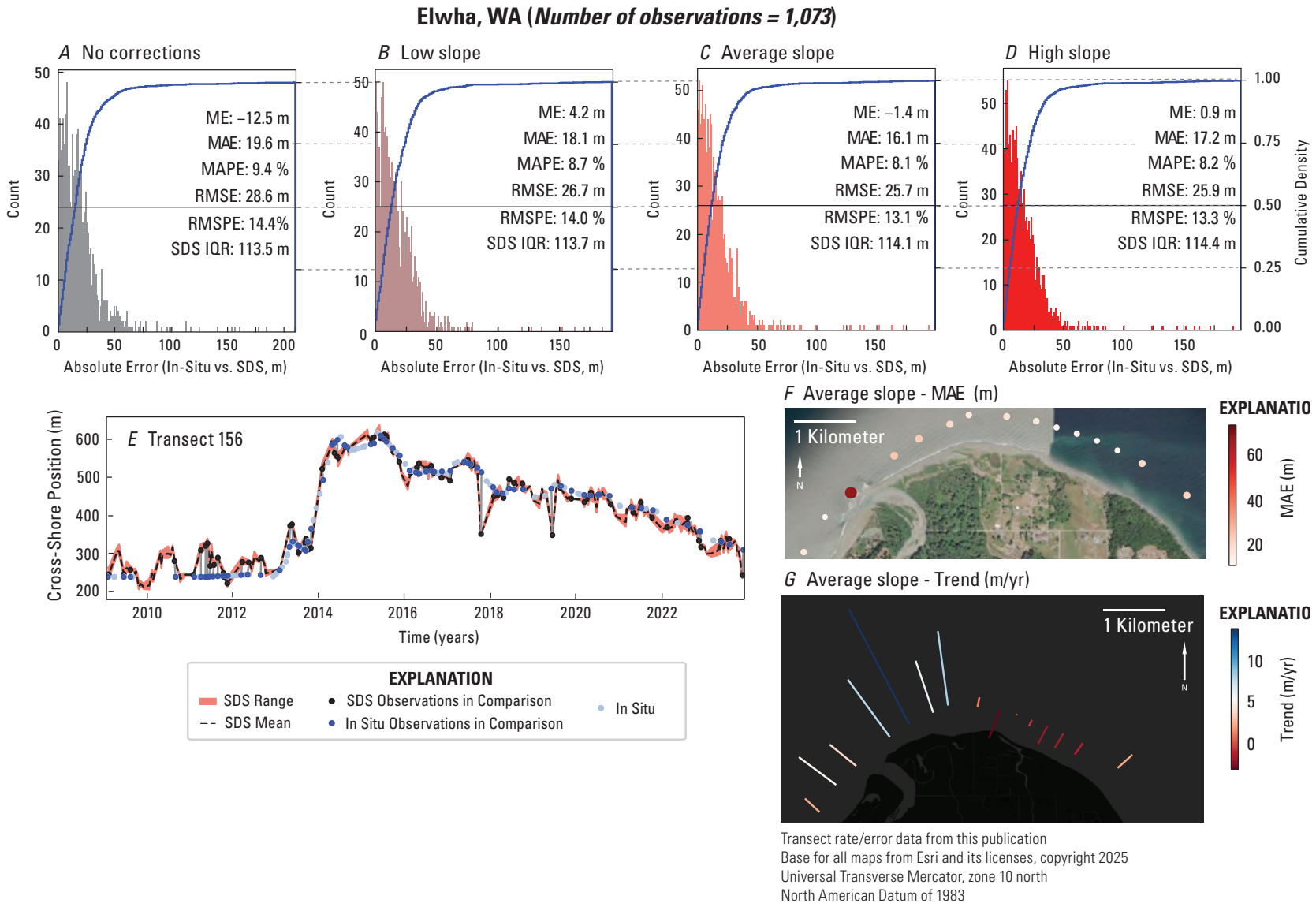

Transect rate/error data from this publication
Base for all maps from Esri and its licenses, copyright 2025
Universal Transverse Mercator, zone 10 north
North American Datum of 1983

Figure 14. Results of error analysis for the Elwha River delta, Washington. Plots showing the distribution of errors between in situ and satellite-derived shoreline (SDS) observations under four scenarios: *A*, no tidal corrections, *B*, low slope, *C*, average slope, and *D*, high slope. *E*, Example timeseries of mean SDS positions and total range at transect 156 during 2009–23. Maps showing *F*, per-transect mean absolute error (MAE) and *G*, linear trends from an average-slope experiment. In situ shoreline data are from Stevens and others (2017) and Miller (2025). Satellite-derived shoreline data are from Buscombe and others (2025). [ME, mean error; m, meter; %, percent; MAPE, mean absolute percentage error; RMSE, root mean squared error; RMSPE, root mean squared percentage error; IQR, interquartile range; vs., versus; km, kilometer; m/yr, meters per year]

about 20 m of observed values under all slope experiments. When the average slope was used, the MAE was 16.1 m. Outliers could be large (up to 300 m), and the resulting distribution skew inflated the accuracy statistics. These large outliers were caused by errors with the CoastSat ML classifier. At this site in particular, the ML classifier often failed to detect sand and water pixels, so a fallback MNDWI thresholding was employed (Fitzpatrick and others, 2024a, b); however, the classifier struggled particularly with (a) shadows on transects southwest of the river mouth; (b) turbidity around the river mouth, which could be excessive during the dam removal process; and (c) the contrast in color and texture between the sand and gravel portions of the shoreline. Per-transect errors were therefore higher on transects near the river mouth and southwest of the river mouth (fig. 14*F*). Despite the outlier noise in the SDS record, trends were captured well in SDS data (figs. 14*E*, 14*G*), showing greatest accretion near the river mouth. This was in part due to the very high number of SDS, approximately 4 per month since 2009. Similar to Barter Island, there were challenges related to the transect-based approach for characterization of shoreline change, given the dynamic changes at this site. Monthly SDS from all data showed this behavior in greater detail and highlighted transitions to more erosional behavior (fig. 15*B*).

Use of a scalar beach slope may have been problematic because of the convex-upward profile shape at this site, which meant the slope tended to steepen landwards. Therefore, a lower datum, such as mean low water (MLW), may be a better shoreline contour for future SDS work because that portion of the beach face may be more linear, and horizontal corrections would be smaller in magnitude. Time-varying and space-varying slope changes may have accounted for some error in this generally steep but variable mesotidal environment, and these changes could be addressed in a future study. We have adapted CoastSeg to be able to import a database of slope values per transect and period, so this adaptation could be used for spatiotemporal slope water level corrections in the future. The cliff shadow effect was most evident in winter (November through March) and caused shorelines to be detected more inland because the shadows were classified as water. With reference to figure 16, shorelines in the eastern portion of the study area, unaffected by shadows, showed no systematic tendency with month of year and water level (figs. 16*A*, 16*C*), whereas those in the western portion affected by shadows in winter showed a systematic landward bias in winter at all water levels (figs. 16*B*, 16*D*). The shadow effect was a classifier failure and could be potentially addressed in the future by customizing the ML classifier for use at this specific site.

5.5. Madeira Beach

No significant challenges were encountered when extracting SDS data for Madeira Beach, and as such, many CoastSeg extraction settings were left at default settings (table 2). Challenges were expected with clouds and weather, but with the large amount of available imagery, clouds did not adversely affect the amount of usable data.

There was a total of 110 usable SDS, 43 in situ shorelines, and 23 in situ shorelines within 10 days of an SDS between 2016 and 2023 (table 1). The Madeira Beach site was a stable and highly managed beach with negligible to small erosional trends in comparison SDS (fig. 17), though LOESS filtered data showed areas of accretionary behavior and an erosion event over much of the site (fig. 18*B*). Most errors were less than 15 m (figs. 17*A–D*), and per-transect error appeared to be randomly distributed; however, the MAE and RMSE were roughly commensurate with the IQR of SDS, suggesting a low signal-to-noise ratio. As a highly managed beach, Madeira Beach was nourished on a routine cycle, reducing detectable signal. Notably, the absence of tidal corrections yielded the strongest results and lowest error in this setting, likely because of the low tidal range; however, differences in error between all four experiments were small (on the order of 1 m or less).

Overall small mixed accretion and erosion was shown in the LOESS filtered data (fig. 18*B*). Despite the managed nature of the beach and low signal-to-noise ratio, certain areas displayed enduring patterns of erosion and accretion, particularly around the 50 m, 150 m, and 250 m marks (fig. 18). These observed fluctuations in shoreline dynamics may have been influenced by the positioning of transects in relation to the existing concrete groins, leading to a complex interplay between structural interventions and natural beach processes. For example, the transect at the 150 m mark showed the largest accretionary trend (figs. 17*H*, 18*B*) and was situated between two groins, whereas nearby transects showing erosion trends were located nearer adjacent groins. Erosion across much of the beach was observed at the end of 2023 (fig. 18*B*), which may have been due to a very active hurricane season for Florida; 20 named tropical storms formed in the Atlantic basin that year, ranking 2023 the fourth most active year for the Atlantic Ocean on record (National Oceanic and Atmospheric Administration, 2023). These events may also have driven the linear trends over this period.

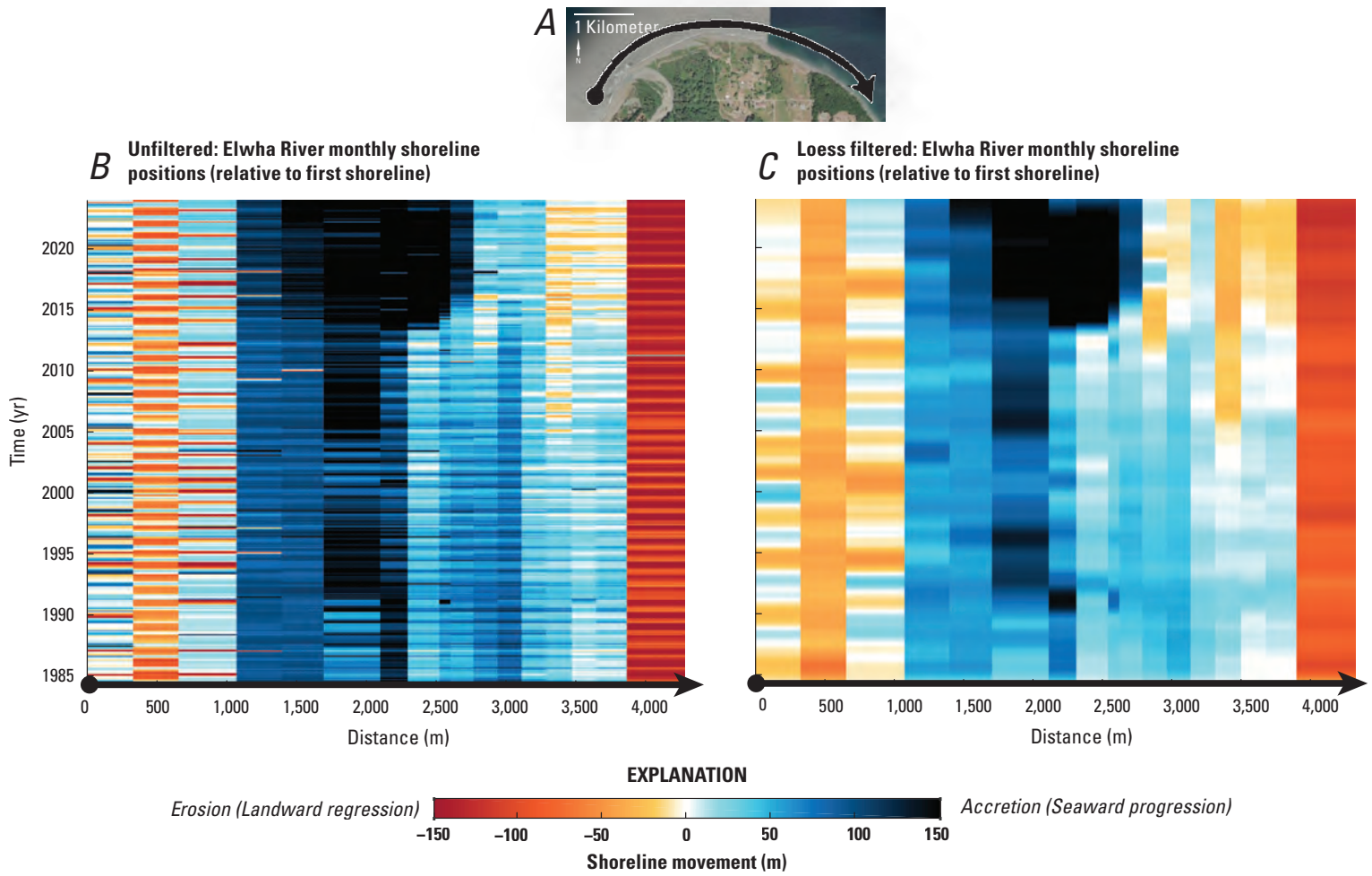

Base for all maps from Esri and its licenses, copyright 2025
Universal Transverse Mercator, zone 10 north
North American Datum of 1983

Figure 15. Monthly resampled locally estimated scatterplot smoothing (LOESS) shoreline positions for the Elwha River delta, Washington, 1984–2022, shown with respect to the 1984 shoreline position: *A*, study area location and orientation, *B*, shoreline positions without filter, and *C*, positions with low-pass filter. Satellite-derived shoreline data are from Buscombe and others (2025). [km, kilometer; yr, year; m, meter]

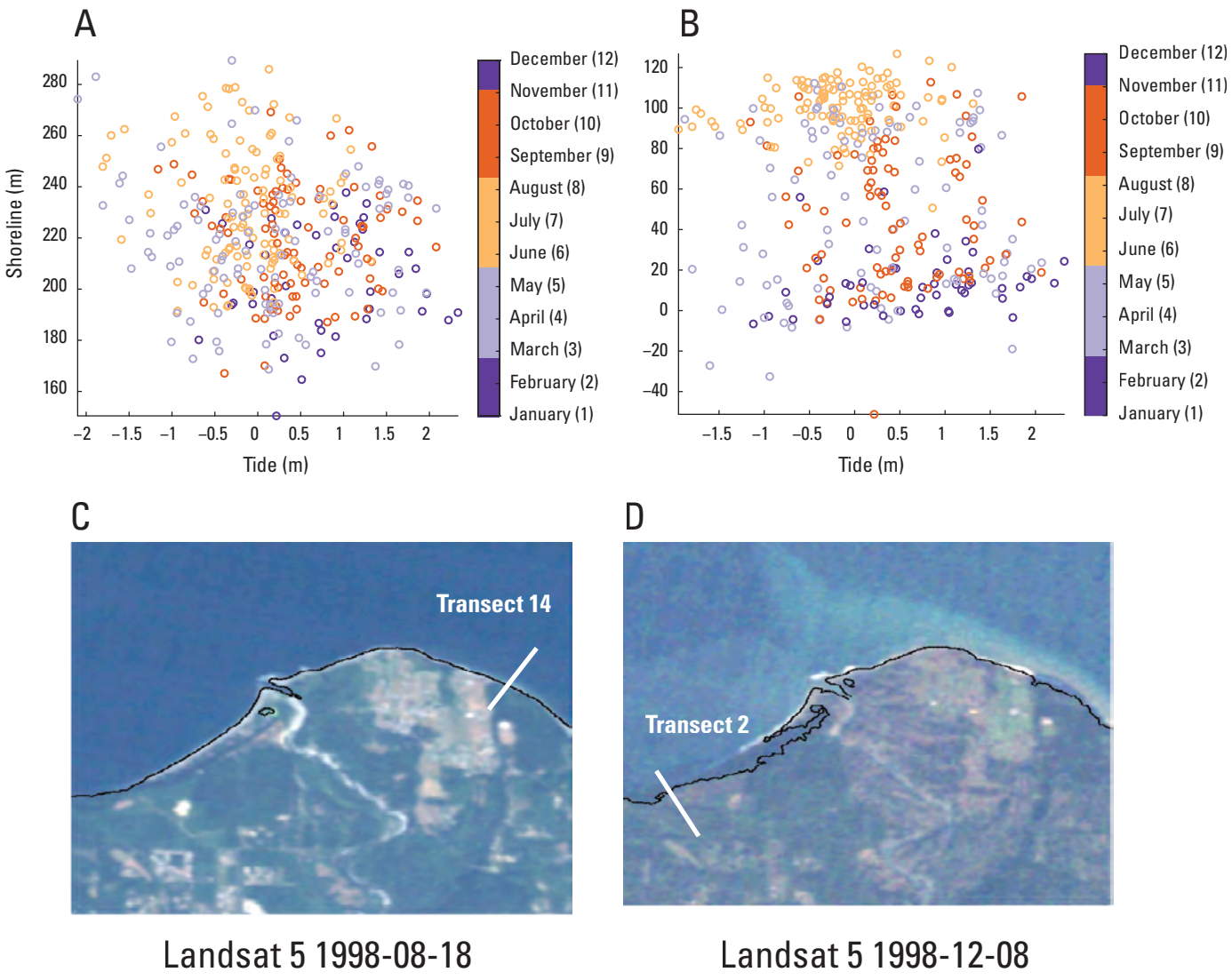

Figure 16. Difference in shoreline positions at the Elwha River delta, Washington, based on season and month at two transects of interest. Plots comparing tide to shoreline position at *A*, transect 14 and *B*, transect 2. Maps showing Landsat 5 imagery (U.S. Geological Survey, 2020a) of *C*, transect 14 in summer (August 18, 1998) and *D*, transect 2 in winter (December 8, 1998). Satellite-derived shoreline data are from Buscombe and others (2025).

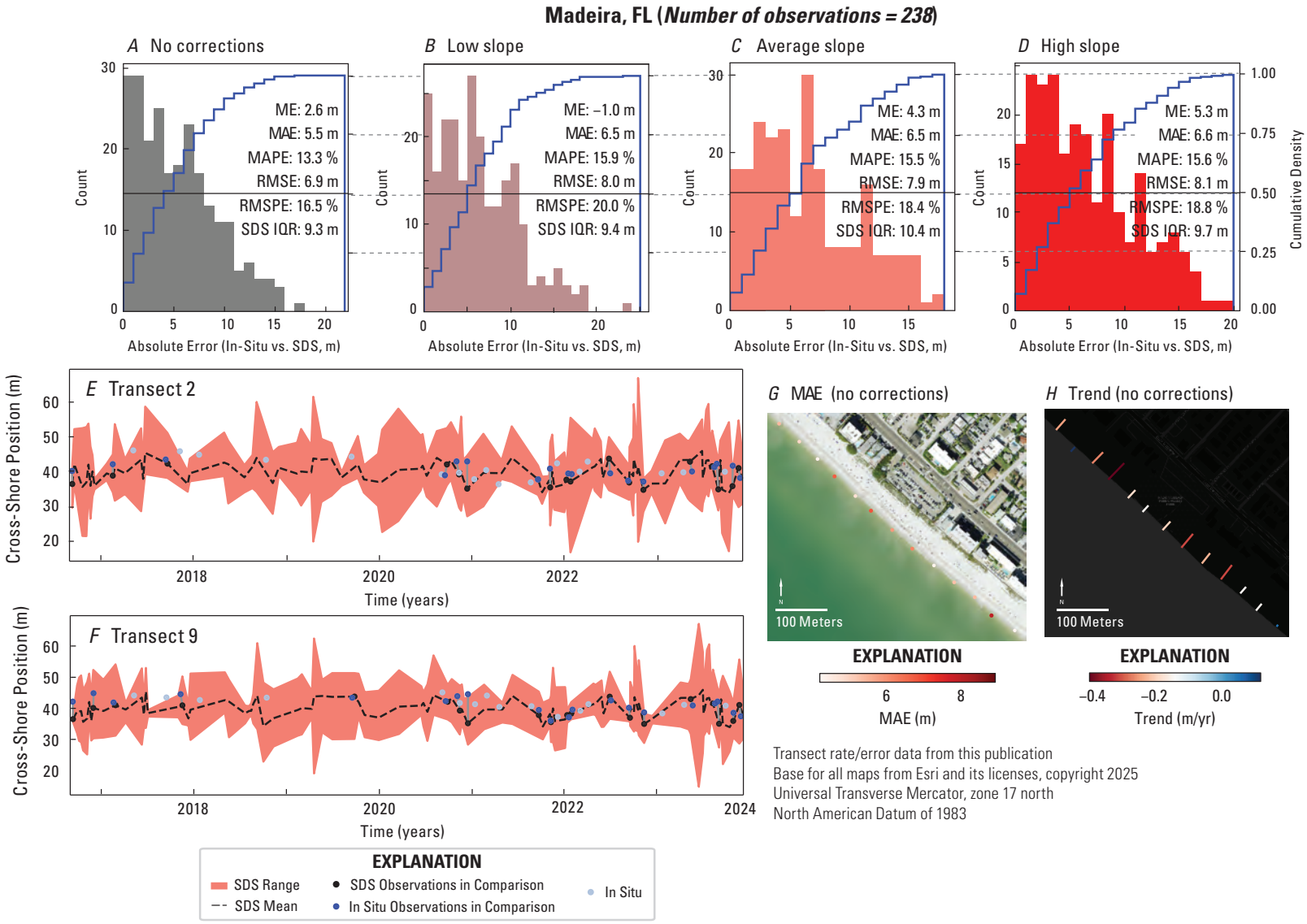

Transect rate/error data from this publication
Base for all maps from Esri and its licenses, copyright 2025
Universal Transverse Mercator, zone 17 north
North American Datum of 1983

Figure 17. Results of error analysis for Madeira Beach, Florida. Plots showing the distribution of errors between in situ and satellite-derived shoreline (SDS) observations under four scenarios: *A*, no tidal corrections, *B*, low slope, *C*, average slope, and *D*, high slope. Example timeseries of mean SDS positions and total range at *E*, transect 2 and *D*, transect 9 during 2016–24. Maps showing *G*, per-transect mean absolute error (MAE) and *H*, linear trends from an average-slope experiment. In situ shoreline data are from Brown and others (2018). Satellite-derived shoreline data are from Buscombe and others (2025). [ME, mean error; m, meter; %, percent; MAPE, mean absolute percentage error; RMSE, root mean squared error; RMSPE, root mean squared percentage error; IQR, interquartile range; vs., versus; km, kilometer; m/yr, meters per year]

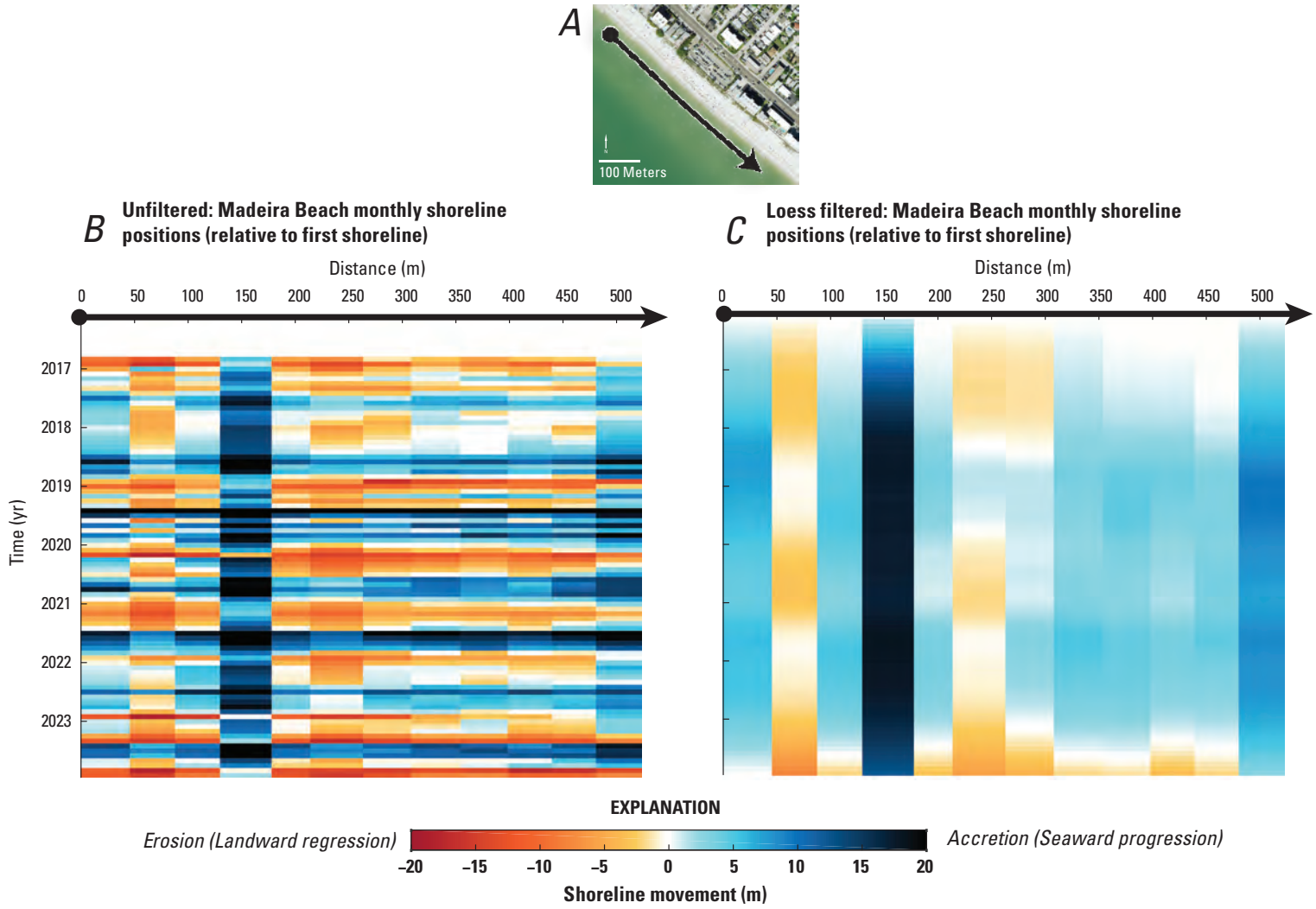

Base for all maps from Esri and its licenses, copyright 2025
Universal Transverse Mercator, zone 17 north
North American Datum of 1983

Figure 18. Monthly resampled locally estimated scatterplot smoothing (LOESS) shoreline positions for Madeira Beach, Florida, 2016–23, shown with respect to the 2016 shoreline position: *A*, study area location and orientation, *B*, shoreline positions without filter, and *C*, positions with low-pass filter. Satellite-derived shoreline data are from Buscombe and others (2025). [yr, year; m, meter]

5.6. Rincón

The Rincón site provided an opportunity to evaluate the skill of CoastSeg:CoastSat for SDS estimation in reef-fronted beach areas. Obtaining a complete record of imagery for this site was a challenge; 30 percent of available satellite imagery was unusable because of cloud cover, incomplete coverage, and other image quality issues, reducing the number of usable shorelines at the site compared to other locations.

There were around 150 SDS from remaining imagery, 17 in situ shorelines, and only 2 in situ shorelines within 10 days of an SDS between 2012 and 2023 (table 1). Linear trends from comparison SDS showed a more mixed pattern than broad erosional trends from in situ data (fig. 19*H*); this disparity may have been due to the limited comparisons available at this site. LOESS-filtered data from all SDS, however, showed more broad erosional behavior and localized bands of accretion over the study period (fig. 20*B*). Errors were generally less than 20 m (fig. 19), and per-transect errors were distributed randomly; however, except for the low-slope scenario, MAE and RMSE were similar to the IQR of SDS observations, suggesting a low signal-to-noise ratio. Of note, the low-slope tidal corrections experiment was most accurate and resulted in much lower error than the other slope experiments; MAE and RMSE for the low-slope scenario were approximately half the values for the no slope or other slope scenarios. Because we lacked sufficient comparison data to investigate, more in situ data or proxy-datum bias corrections would be needed to further explain these results.

The coral reefs did not affect the ability of CoastSeg to derive shorelines from satellite imagery. Although there were few observations before 1999, enough SDS were available after L7 imagery became available to support monthly observations (fig. 20). Erosional trends were broadly observed across the shoreline, but the middle of the Rincón coastline showed the greatest erosion, matching erosion hotspots from in situ data. The highest erosion was around the 2,800 m mark (fig. 20). The second-highest erosion was seen at the 600 m mark in the southern portion of the study area (fig. 20). Both erosion areas were coastal sections with relatively wider sandy beaches without coastal structures or buildings. Two areas adjacent to the central erosional hotspot (around the 2,400 m and 4,700 m marks) showed consistent accretion in monthly plots (fig. 20), which generally matched long-term trend data.

5.7. Time and File Size Usage

Details on time and data storage needed to prepare and process data at all sites were noted to understand what may be required to develop a workflow for other sites. In this section, information associated with the image extraction for Barter Island is discussed throughout because it is representative of the maximum range of time and storage needed to complete work for this study. All other sites required less time and file space, pending availability of imagery and challenges with extraction.

Several weeks were needed to fully set up ROIs, transects, and reference shorelines for Barter Island, but much of that time was spent becoming familiar with the CoastSeg software, file formatting requirements, and working with the developers on software improvements. As much as a full workday (8–10 hours) was needed just to manually screen and filter out bad imagery and initial detections, and more ROIs (greater area) required more time. Once personnel are familiar with the CoastSeg software and workflow, this time could be significantly reduced to only 1 or 2 weeks to fully set up, refine settings, and filter imagery or detections, even for the most challenging sites like Barter Island.

Work was done on a desktop computer with sufficient storage and processing capability for scientific processing. The amount of storage needed for SDS data depends on the size of the study area, the period of interest, and the satellites used. At Barter Island, sessions for raw (non-tidally corrected) and one tidal correction for all four ROIs over the entire study period (1984–2023) required 29 gigabytes (GB) to store the Landsat imagery. Because this site also required the use of Sentinel-2 imagery, the amount of storage space used by downloaded data increased to approximately 40 GB. In total, shoreline detections and associated output required about 1,200 megabytes (MB), of which the Landsat imagery accounted for around 900 MB. Thus, about 31 GB of space was needed for a Landsat workflow at Barter Island; this included downloaded imagery underpinning the final datasets, as well as bad imagery, bad detections, supporting files, and all session output. Again, this estimate represents the upper end of file size requirements. The other locations needed less storage space.

6.0. Discussion

Positional error is large enough at Barter Island, Cape Cod, the Elwha River delta, and Rincón that using individual, discrete SDS in other assessments and work is challenging (figs. 7, 11, 14, 17, and 19; summarized in table 5). The larger random error makes SDS less than ideal for analysis of discrete time instances. There are additional challenges with transect-based approaches in dynamic sites such as Barter Island and the Elwha River delta. However, despite these challenges and positional errors, trends of shoreline change are well illustrated. Short-term rates derived from SDS were similar to in situ rates at 84 percent of transects across all sites (figs. 7, 11, 13, 14, 17, and 19; tables 3, 4). SDS offers the added benefit of orders-of-magnitude more data in timeseries, providing the opportunity to understand shoreline responses and complex behavior beyond linear rates of change and influenced by multiple drivers and scales of forcing. Filtering and data preparation, as conducted in this paper, can be

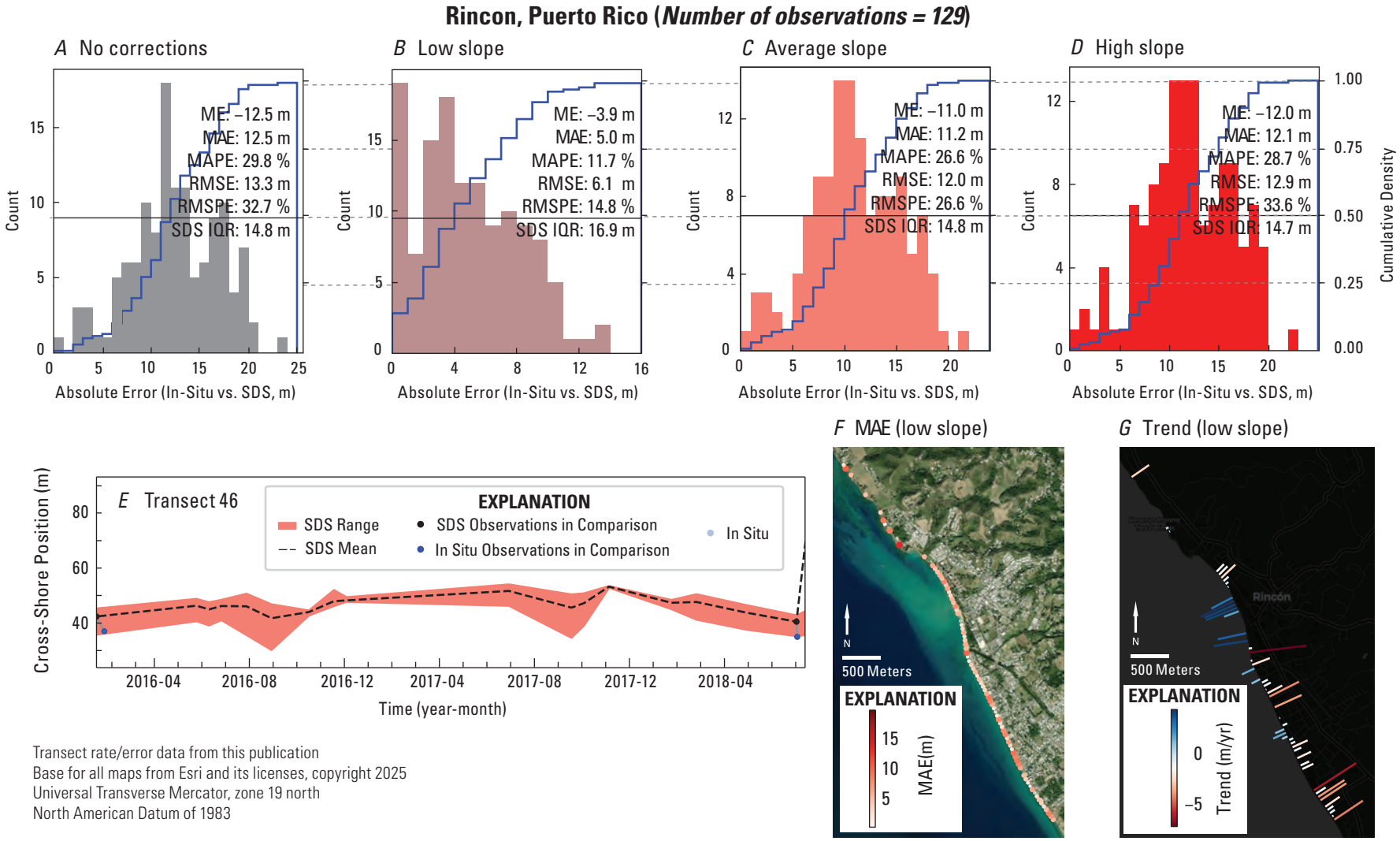

Transect rate/error data from this publication
Base for all maps from Esri and its licenses, copyright 2025
Universal Transverse Mercator, zone 19 north
North American Datum of 1983

Figure 19. Results of error analysis for Rincón, Puerto Rico. Plots showing the distribution of errors between in situ and satellite-derived shoreline (SDS) observations under four scenarios: *A*, no tidal corrections, *B*, low slope, *C*, average slope, and *D*, high slope. *E*, Example timeseries of mean SDS positions and total range at transect 46 during 2016–18. Maps showing *F*, per-transect mean absolute error (MAE) and *G*, linear trends from a low-slope experiment. In situ shoreline data are from Henderson and others (2021). Satellite-derived shoreline data are from Buscombe and others (2025). [ME, mean error; m, meter; %, percent; MAPE, mean absolute percentage error; RMSE, root mean squared error; RMSPE, root mean squared percentage error; IQR, interquartile range; vs., versus; UTC, Coordinated Universal Time; m/yr, meters per year]

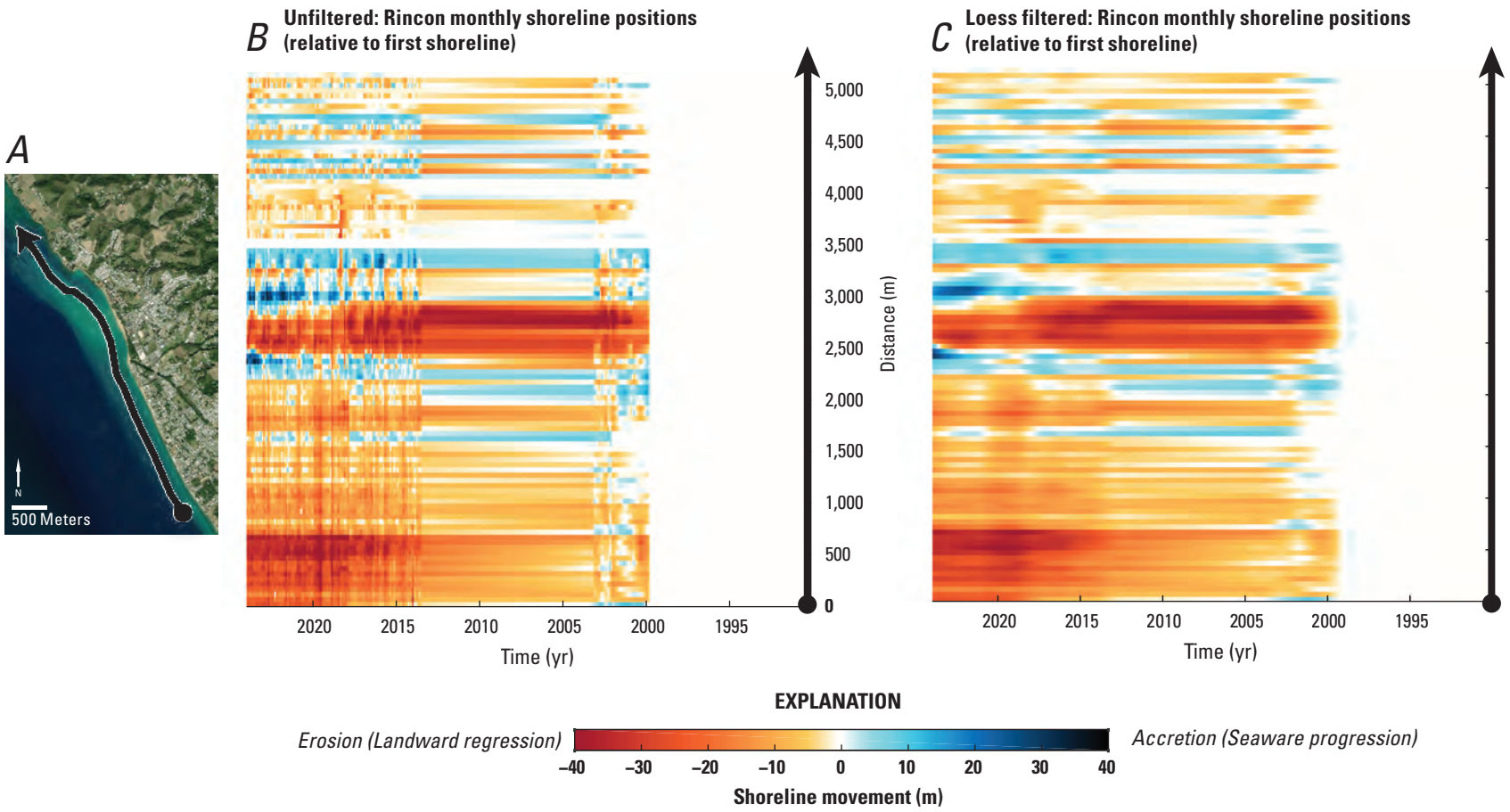

Base for all maps from Esri and its licenses, copyright 2025
Universal Transverse Mercator, zone 19 north
North American Datum of 1983

Figure 20. Monthly resampled locally estimated scatterplot smoothing (LOESS) shoreline positions for Rincón, Puerto Rico, 1987–2023, shown with respect to the 1987 shoreline position: *A*, study area location and orientation, *B*, shoreline positions without filter, and *C*, positions with low-pass filter. Satellite-derived shoreline data are from Buscombe and others (2025). [km, kilometer; yr, year; m, meter]

Table 5. Summary of root mean square error (RMSE) and interquartile range (IQR) values for all sites for different satellite-derived shoreline tidal corrections.

[m, meter]

Location	No tidal correction		Low slope		Average slope		High slope	
	RMSE (m)	IQR (m)	RMSE (m)	IQR (m)	RMSE (m)	IQR (m)	RMSE (m)	IQR (m)
Barter Island	29.6	433.3	30.9	434.8	29.6	433.4	29.7	433.3
Cape Cod	14.3	26.7	11.7	29.5	9.9	24.3	10.4	24.9
Elwha River delta	28.6	113.5	26.7	113.7	25.7	114.1	25.9	114.4
Madeira Beach	6.9	9.3	8.0	9.4	7.9	10.4	8.1	9.7
Rincón	13.3	14.8	6.1	16.9	12.0	14.8	12.9	14.7

automated to extract shoreline behavior (rather than individual positions) for assessments or to supplement in situ data. This includes behavior on the order of annual, seasonal, and monthly scales, as well as significant episodic changes, at the alongshore horizontal resolution in this study (about 50 m). Even for the most challenging locations, usable data can still be extracted, as illustrated by the Barter Island dataset. Additionally, models that include data assimilation techniques capable of accounting for such error, such as Vitousek and others (2023b, 2024), are ideal to leverage this data because they use the high temporal resolution and wide geographic coverage of available geospatial data.

Use of an average slope is appropriate for most sites, at least as a starting point (table 5). Adjusting scalar slopes for spatial or temporal variability yields marginal improvements, if any. Rincón is an exception, but the cause could not be determined during this effort because of limited data. Approaches to tidally correct shorelines using transect-specific slopes (such as those of Vos and others, 2020) or time-varying slopes are also available, may offer advantages for specific areas (for example, the Elwha River delta), and could provide additional improvements over scaler slope methods, which could be clarified with further study.

Computing intersections (an underlying CoastSat function; Vos and others, 2019b) is relatively slow and requires multiple site-specific parameters, such as the inland distance, variability limits, and a minimum point count to identify shoreline-transect intersections. The method works by selecting nearby shoreline points, excluding those too far inland, and using the median position of the remaining points as the intersection if they meet quality thresholds. However, the method can be inefficient because it requires manual tuning and often fails to filter out outliers effectively. This method could be simplified to reduce the need for fine-tuning, improve processing speed, and enhance its reliability across diverse coastal environments.

Setting up the geometry of ROIs and transects requires dedicated preparation, especially in complex areas, and may require overlapping ROIs (as discussed in section 5.2) to yield reliable and complete data along the boundaries. Any regional expansion of SDS generation would necessitate thorough preparation of transects and ROIs and an iterative refinement of settings to get consistent data. Site-specific phenomena (like shadows) should be considered in any regional implementation and may require detailed investigation.

Using time and file size in this work as benchmarks, we estimate that 3–4 weeks of dedicated time would be required to fully set up, refine settings, and filter images or detections for the full satellite record in a new, challenging region on the scale of 100 km; however, the time requirement could be much shorter in a less-complex environment. For 40 years of imagery, associated file sizes would be 80–170 GB of downloaded imagery (dependent on the complexity of the coastline, ROIs, and available satellite imagery) and 4–5 GB of extracted shoreline data per 100 km. Desktop computers with storage and processing capabilities sufficient for scientific work can easily support this at regional scales, but larger scales may be better supported by cloud or other storage solutions. Use of High-Performance Computing resources for workflow processing was not investigated in this study but could similarly support work at larger geographic scales. Improvements in image classification, bad image detection, and bad shoreline detection could drastically improve efficiency and consistency of data and reduce the time required for manual filtering, supporting expansion efforts, especially in challenging environments. Setup represents the bulk of the time required to invest in any expansion effort. Once time is invested for setup, new data acquisition and feature detection on a routine basis would be on the order of minutes, especially with the improvements listed above. Additionally, such routine updates to data could theoretically be automated.

As done in this effort, the use of scripted filters to process resulting SDS data for analysis and use with other data types is critical, and these filters can be automated or incorporated into a workflow. Such efforts could yield a robust dataset showing detailed episodic to annual behavior and trends across large sections of coastline. These processed data can supplement in situ records, support data-assimilating shoreline forecast models and forecasts, and provide valuable insight in data-poor regions.

Although this effort focused on comparisons of MSL and MHW shorelines, it would be straightforward to extract multiple or additional shoreline representations with the CoastSeg:CoastSat implementation to better support end-user needs.

The close collaboration between users and developers resulted in substantial improvements to the CoastSeg:CoastSat workflow. Several features were added to CoastSeg as a result of consistent, iterative feedback on using the workflow in varied environments, including (a) representing the shoreline extraction area as a editable polygon on the map to help avoid extracting shorelines from the back barrier shorelines or ponds; (b) being able to sort images into good and bad folders to avoid having to manually delete the files from which users did not want shorelines extracted; (c) automatically deleting images containing excessive cloud cover during the download process, reducing time spent on manual sorting; and (d) plotting the reference shoreline buffer on the extracted shoreline detection figures to facilitate optimal size determination. These small improvements were achieved through close partnership and co-development and represent significant gains in efficiency of the workflow and a reduction in manual requirements.

7.0. Summary

Shoreline data extracted from satellite imagery using automated tools and techniques have the potential to be transformative in coastal research, monitoring, and hazard projections, but operationalization of the workflows for regional monitoring necessitates careful validation of the software and data infrastructure. We used the software to generate 40-year SDS timeseries at five sites representing a wide range of geological, hydrodynamic, and morphodynamic settings across the United States with the goal of exploring the viability and accuracy of the CoastSeg:CoastSat workflow for large-scale satellite-derived shoreline (SDS) mapping. The SDS positions and rates of change were compared to traditionally sourced shorelines and change rate data. Previous SDS validations have focused exclusively on the random error of SDS data, but we also reported statistics related to shoreline variability and considered factors such as software usability, storage capacity, and processing requirements for large-scale mapping.

Workflow settings were refined for each site's specific challenges, and SDS were extracted and tidally corrected as described in section 4.0. SDS were then compared to in situ shoreline data; comparisons were made only using SDS occurring closely in time to traditionally sourced in situ data, using filters to address outliers. Error statistics relating to shoreline position variability were reported and inspected. All SDS data were plotted to show monthly changes and shoreline behavior over the entire study periods. Other factors, including software usability and storage and computation requirements for large-scale mapping, were also noted.

Results show that, although SDS positional error is too large to use discrete or individual SDS in analysis, shoreline behavior and trends are captured well. Adequate data preparation and filtering are necessary to get quality and consistent data, but the process can be automated. Average slope values for scaler slope tidal corrections are sufficient for most locations. Setting up and refining program settings for each site represented the largest usage of time (multiple weeks), and should be considered for any expansion; however, once set up, data collection is comparatively negligible (on the order of minutes). Data and computation requirements for regional uses can be supported by desktop computers, but cloud options or robust storage solutions may be considered for larger than regional scales.

Acknowledgments

We would like to thank the reviewers for their thorough and thoughtful feedback. We are also grateful to the U.S. Geological Survey Science Publishing Network for their patience and knowledge to help prepare this manuscript.

References Cited

Almeida, L.P., Efraim de Oliveira, I.E., Lyra, R., Scaranto Dazzi, R.L, Martins, V.G., and Fontoura Klein, A.H.da, 2021, Coastal Analyst System from Space Imagery Engine (CASSIE)—Shoreline management module: Environmental Modelling & Software, v. 140, accessed June 1, 2025, at https://doi.org/10.1016/j.envsoft.2021.105033.

Berman, G., 2011, Longshore sediment transport, Cape Cod, Massachusetts: Woods Hole Sea Grant Program and Barnstable Country's Cape Cod Cooperative Extension, 46 p., accessed June 1, 2025, at https://repository.library.noaa.gov/view/noaa/34878/noaa_34878_DS1.pdf.

Bishop-Taylor, R., Nanson, R., Sagar, S., and Lymburner, L., 2021, Mapping Australia's dynamic coastline at mean sea level using three decades of Landsat imagery: Remote Sensing of Environment, v. 267, accessed June 1, 2025, at https://doi.org/10.1016/j.rse.2021.112734.

Brown, J.A., Birchler, J.J., Thompson, D.M., Long, J.W., and Seymour, A.C., 2018, Beach profile data collected from Madeira Beach, FL (ver. 5.0, April 2024): U.S. Geological Survey data release, accessed June 1, 2025, at https://doi.org/10.5066/F7T43S94.

Buscombe, D., and Fitzpatrick, S., 2023, CoastSeg: Beach transects and beachface slope database v1.0: Zenodo dataset, accessed June 1, 2025, at https://doi.org/10.5281/zenodo.8187949.

Buscombe, D., Burgess, J., Doran, K., Batiste, S., Gibbs, A., Henderson, R., Heslin, J., Janda, C., Lundine, M., O'Neill, A.C., Terrano, J., Warrick, J., and Weber, K., 2025, Satellite-derived shorelines from CoastSeg in multiple U.S. locations (1984–2023): U.S. Geological Survey data release, accessed June 1, 2025, at https://doi.org/10.5066/P1NUEFDP.

Butler, H., Daly, M., Doyle, A., Gillies, S., Schaub, T., and Hagen, S., 2016, The GeoJSON format (RFC 7946): Internet Engineering Task Force, accessed June 1, 2025, at https://tools.ietf.org/html/rfc7946.

Castelle, B., Masselink, G., Scott, T., Stokes, C., Konstantinou, A., Marieu, V., and Bujan, S., 2021, Satellite-derived shoreline detection at a high-energy meso-macrotidal beach: Geomorphology, v. 383, accessed June 1, 2025, at https://doi.org/10.1016/j.geomorph.2021.107707.

Castelle, B., Kras, E., Masselink, G., Scott, T., Konstantinou, A., and Luijendijk, A., 2024, Satellite-derived sandy shoreline trends and interannual variability along the Atlantic coast of Europe: Scientific Reports, v. 14, no. 1, accessed June 1, 2025, at https://doi.org/10.1038/s41598-024-63849-4.

Crowell, M., Leatherman, S., and Buckley, M., 1991, Historical shoreline change: error analysis and mapping accuracy: Journal of Coastal Research, v. 7, p. 839-852, accessed September 1, 2025, at https://www.jstor.org/stable/4297899.

Doran, K.S., Birchler, J.J., and Pardun, J.M., 2017, 2018 Puerto Rico USACE lidar-derived dune crest, toe and shoreline (ed. 5), *in* Doran, K.S., Long, J.W., Birchler, J.J., Brenner, O.T., Hardy, M.W., Morgan, K.L.M., Stockdon, H.F., and Torres, M.L., comps., Lidar-derived beach morphology (dune crest, dune toe, and shoreline) for U.S. sandy coastlines (ver. 6.0, March 2024): U.S. Geological Survey data release, accessed June 1, 2025, at https://doi.org/10.5066/F7GF0S0Z.

Erikson, L.H., Gibbs, A.E., Richmond, B.M., Storlazzi, C.D., Jones, B.M., and Ohman, K., 2020, Changing storm conditions in response to projected 21st century climate change and the potential impact on an Arctic barrier island–Lagoon system—A pilot study for Arey Island and Lagoon, Eastern Arctic Alaska: U.S. Geological Survey Open-File Report 2020–1142, 68 p., accessed June 1, 2025, at https://doi.org/10.3133/ofr20201142.

European Space Agency, 2017, Sentinel-2 product collection: Copernicus Data Space Ecosystem webpage, accessed June 1, 2025, at https://dataspace.copernicus.eu/explore-data/data-collections/sentinel-data/sentinel-2.

Farris, A.S., Weber, K.M., Doran, K.S., and List, J.H., 2018, Comparing methods used by the US Geological Survey Coastal and Marine Geology Program for deriving shoreline position from lidar data: U.S. Geological Survey Open-File Report 2018–1121, accessed June 1, 2025, at https://doi.org/10.3133/ofr20181121.

Farris, A.S., Weber, K.M., and List, J.H., 2020, Mean high water shorelines for the Outer Cape of Massachusetts from Nauset Inlet to Race Point (1998–2005): U.S. Geological Survey data release, accessed June 1, 2025, at https://doi.org/10.5066/P9GWL52F.

Fisher, J.J., and Leatherman, S.P., 1987, Glacial and coastal geology, Cape Cod National Seashore—Massachusetts, chaps. 47–48 *of* Roy, D.C., ed., Northeastern Section of the Geological Society of America—Centennial field guide volume 5: Boulder, Colo., Geological Society of America, Inc., accessed June 1, 2025, at https://doi.org/10.1130/0-8137-5405-4.213.

Fitzpatrick, S., Buscombe, D., Warrick, J.A., Lundine, M.A., and Vos, K., 2024a, CoastSeg—An accessible and extendable hub for satellite-derived-shoreline (SDS) detection and mapping (ver. 1.2.9, June 2024): Zenodo dataset, accessed June 1, 2025, at https://doi.org/10.5281/zenodo.12555413.

Fitzpatrick, S., Buscombe, D., Warrick, J.A., Lundine, M.A., and Vos, K., 2024b, CoastSeg—An accessible and extendable hub for satellite-derived-shoreline (SDS) detection and mapping: Journal of Open Source Software, v. 9, no. 99, 9 p., accessed June 1, 2025, at https://doi.org/10.21105/joss.06683.

Gelfenbaum, G., Stevens, A.W., Miller, I., Warrick, J.A., Ogston, A.S., and Eidam, E., 2015, Large-scale dam removal on the Elwha River, Washington, USA—Coastal geomorphic change: Geomorphology, v. 246, p. 649–668, accessed June 1, 2025, at https://doi.org/10.1016/j.geomorph.2015.01.002.

Gibbs, A.E., Nolan, M., and Snyder, A.G., 2019a, Orthophotomosaics, elevation point clouds, digital surface elevation models and supporting data from the north coast of Barter Island, Alaska: U.S. Geological Survey data release, accessed June 1, 2025, at https://doi.org/10.5066/P9964TKX.

Gibbs, A.E., Snyder, A.G., and Richmond, B.R., 2019b, National Assessment of shoreline change—Historical shoreline change along the north coast of Alaska, Icy Cape to Cape Prince of Wales: U.S. Geological Survey Open File Report 2019–1146, 52 p., accessed June 1, 2025, at https://doi.org/10.3133/ofr20191146.

Gibbs, A.E., Jones, B.M., and Richmond, B.M., 2020, A GIS compilation of vector shorelines and coastal bluff edge positions, and associated rate-of-change data for Barter Island, Alaska: U.S. Geological Survey data release, accessed June 1, 2025, at https://doi.org/10.5066/P9CRBC5I.

Gibbs, A.E., Erikson, L.H., Jones, B.M., Richmond, B.M., and Engelstad, A.C., 2021, Seven decades of coastal change at Barter Island, Alaska—Exploring the importance of waves and temperature on erosion of coastal permafrost bluffs: Remote Sensing (Basel), v. 13, no. 21, 25 p., accessed June 1, 2025, at https://doi.org/10.3390/rs13214420.

Giese, G.S., Adams, M.B., Rogers, S.S., Dingman, S.L., Borrelli, M., and Smith, T.L., 2011, Coastal sediment transport on outer Cape Cod, Massachusetts—Observation and theory, *in* Wang, P., Rosati, J.D., and Roberts T.M., eds., The Proceedings of the Coastal Sediments 2011: Hackensack, N.J., World Scientific Publishing Co. Pte. Ltd., v. 3, p. 2353–2356, accessed June 1, 2025, at https://doi.org/10.1142/9789814355537_0176.

Gorelick, N., Hancher, M., Dixon, M., Ilyushchenko, S., Thau, D., and Moore, R., 2017, Google Earth Engine—Planetary-scale geospatial analysis for everyone: Remote Sensing of Environment, v. 202, p. 18–27, accesssed September 26, 2025, at https://doi.org/10.1016/j.rse.2017.06.031.

Hapke, C.J., Himmelstoss, E.A., Kratzmann, M.G., List, J.H., and Thieler, E.R., 2011, National assessment of shoreline change—Historical shoreline change along the New England and Mid-Atlantic coasts: U.S. Geological Survey Open File Report 2010–1118, 57 p., accessed June 1, 2025, at https://doi.org/10.3133/ofr20101118.

Henderson, R.E., Heslin, J.L., and Himmelstoss, E.A., 2021, Puerto Rico shoreline change—A GIS compilation of shorelines, baselines, intersects, and change rates calculated using the Digital Shoreline Analysis system version 5.1 (ver. 2.0, March 2023): U.S. Geological Survey data release, accessed June 1, 2025, at https://doi.org/10.5066/P9FNRRN0.

Hess, A., Iyer, H., and Malm, W., 2001, Linear trend analysis—A comparison of methods: Atmospheric Environment, v. 35, no. 30, p. 5211–5222, accessed June 1, 2025, at https://doi.org/10.1016/S1352-2310(01)00342-9.

Himmelstoss, E.A., Farris, A.S., Henderson, R.E., Kratzmann, M.G., Ergul, A., Zhang, O., Zichichi, J.L., and Thieler, E.R., 2018, DSAS (ver. 5.1, 2021): U.S. Geological Survey software release, accessed June 1, 2025, at https://code.usgs.gov/cch/dsas.

Hoover, D.J., Snyder, A.G., Barnard, P.L., Hansen, J.E., and Warrick, J.A., 2024, Shoreline data for Ocean Beach, San Francisco, California, 2004 to 2021: U.S. Geological Survey data release, accessed June 1, 2025, at https://doi.org/10.5066/P13CAWLM.

Hopkins, D.M., and Hartz, R.W., 1978, Coastal morphology, coastal erosion, and barrier islands of the Beaufort Sea, Alaska: U.S. Geological Survey Open File Report 78-1063, accessed June 1, 2025, at https://doi.org/10.3133/ofr781063.

Janda, C.N., Warrick, J.A., Buscombe, D., and Batiste, S., 2025, Shoreline Change of Western Long Island, New York, from Satellite-Derived Shorelines: Coasts, v. 5, no. 2, 29 p., accessed June 1, 2025, at https://doi.org/10.3390/coasts5010002.

Kratzmann, M.G., 2022, U.S. Geological Survey national shoreline change—Summary statistics for updated vector shorelines (1800s–2010s) and associated shoreline change data for the Georgia and Florida coasts: U.S. Geological Survey Data Report 1156, 8 p., accessed June 1, 2025, at https://doi.org/10.3133/dr1156.

Konstantinou, A., Scott, T., Masselink, G., Stokes, C., Conley, D. and Castelle, B., 2023, Satellite-based shoreline detection for macro-tidal coasts—Impacts of morphological and hydrodynamic setting, *in* Wang, P., Royer, E., and Rosati, J.D., eds., The Proceedings of the Coastal Sediments 2023, p. 1392–1402, accessed June 1, 2025, at https://doi.org/10.1142/9789811275135_0129.

List, J.H., Farris, A.S., and Sullivan, C., 2006, Reversing storm hotspots on sandy beaches—Spatial and temporal characteristics: Marine Geology, v. 226, no. 3-4, p. 261–279, accessed June 1, 2025, at https://doi.org/10.1016/j.margeo.2005.10.003.

Liu, H., Shah, S., and Jiang, W., 2004, On-line outlier detection and data cleaning: Computers & Chemical Engineering, v. 28, no. 9, p. 1635–1647, accessed June 1, 2025, at https://doi.org/10.1016/j.compchemeng.2004.01.009.

Ludka, B.C., Guza, R.T., O'Reilly, W.C., Merrifield, M.A., Flick, R.E., Bak, A.S., Hesser, T., Bucciarelli, R., Olfe, C., Woodward, B., Boyd, W., Smith, K., Okihiro, M., Grenzeback, R., Parry, L., and Boyd, G., 2019, Sixteen years of bathymetry and waves at San Diego beaches: Scientific Data, v. 6, 13 p., accessed June 1, 2025, at https://doi.org/10.1038/s41597-019-0167-6.

Luijendijk, A., Hagenaars, G., Ranasinghe, R., Baart, F., Donchyts, G., and Aarninkhof, S., 2018, The state of the world's beaches: Scientific Reports, v. 8, 11 p., accessed June 1, 2025, at https://doi.org/10.1038/s41598-018-24630-6.

Lyard, F.H., Allain, D.J., Cancet, M., Carrere, L., and Picot, N., 2021, FES2014 global ocean tide atlas—Design and performance: Ocean Science, v. 17, no. 3, p. 615–649, accessed June 1, 2025, at https://doi.org/10.5194/os-17-615-2021.

Mao, Y., Harris, D.L., Xie, Z., and Phinn, S., 2021, Efficient measurement of large-scale decadal shoreline change with increased accuracy in tide-dominated coastal environments with Google Earth Engine: ISPRS Journal of Photogrammetry and Remote Sensing, v. 181, p. 385–399, accessed June 1, 2025, at https://doi.org/10.1016/j.isprsjprs.2021.09.021.

Miller, I.M., Warrick, J.A., and Morgan, C., 2011, Observations of coarse sediment movements on the mixed beach of the Elwha delta, Washington: Marine Geology, v. 282, no. 3–4, p. 201–214, accessed June 1, 2025, at https://doi.org/10.1016/j.margeo.2011.02.012.

Miller, I., 2019, Beach profile data for the Elwha River delta, 2011–2018: PANGAEA—Data Publisher for Earth & Environmental Science dataset, accessed June 1, 2025, at https://doi.org/10.1594/PANGAEA.901486.

Miller, I., 2025, Beach profile data for the Elwha River delta, 2018–2024: PANGAEA—Data Publisher for Earth & Environmental Science dataset, accessed June 1, 2025, at https://doi.org/10.1594/PANGAEA.977774.

Moore, L., 2000, Shoreline mapping techniques: Journal of Coastal Research, v 16, p. 111-124, accessed September 1, 2025, at https://www.jstor.org/stable/4300016.

Muir, F.M.E., Hurst, M.D., Richardson-Foulger, L., Rennie, A.F., and Naylor, L.A., 2024, VedgeSat—An automated, open-source toolkit for coastal change monitoring using satellite-derived vegetation edges: Earth Surface Processes and Landforms, v. 49, no. 8, p. 2405–2423, accessed June 1, 2025, at https://doi.org/10.1002/esp.5835.

National Oceanic and Atmospheric Administration, 2023, 2023 Atlantic hurricane season ranks 4th for most-named storms in a year: National Oceanic and Atmospheric Administration web page, accessed June 1, 2025, at https://www.noaa.gov/news-release/2023-atlantic-hurricane-season-ranks-4th-for-most-named-storms-in-year.

National Oceanic and Atmospheric Administration, 2025, Tides and currents—Prudhoe Bay, AK—Station ID 9497645: National Oceanic and Atmospheric Administration database, accessed January 15, 2025, at http://tidesandcurrents.noaa.gov/stationhome.html?id=9497645.

Otsu, N., 1979, A threshold selection method from gray-level histograms: IEEE Transactions on Systems, Man, and Cybernetics, v. 9, no. 1, p. 62–66, accessed June 1, 2025, at https://doi.org/10.1109/TSMC.1979.4310076.

Ritchie, A.C., Warrick, J.A., East, A.E., Magirl, C.S., Stevens, A.W., Bountry, J.A., Randle, T.J., Curran, C.A., Hilldale, R.C., Duda, J.J., Gelfenbaum, G.R., Miller, I.M., Pess, G.R., Foley, M.M., McCoy, R., and Ogston, A.S., 2018, Morphodynamic evolution following sediment release from the world's largest dam removal: Scientific Reports, v. 8, 13 p., accessed June 1, 2025, at https://doi.org/10.1038/s41598-018-30817-8.

Ruggiero, P., and List, J.H., 2009, Improving accuracy and statistical reliability of shoreline position and change rate estimates: Journal of Coastal Research, v. 255, p. 1069–1081, accessed June 1, 2025, at https://doi.org/10.2112/08-1051.1.

Schwarzman, B., 2002, The nature of Cape Cod: University Press of New England, accessed June 1, 2025, at https://archive.org/details/natureofcapecod00beth/page/n9/mode/2up.

Stevens, A.W., Gelfenbaum, G., Warrick, J.A., Miller, I.M., and Weiner, H.M., 2017, Bathymetry, topography, and sediment grain-size data from the Elwha River delta, Washington (ver. 5.0, November 2024): U.S. Geological Survey data release, accessed June 1, 2025, at https://doi.org/10.5066/F72N51GC.

Thieler, E.R., Rodríguez, R.W., and Carolo, M., 1995, Beach erosion and coastal development at Rincon, Puerto Rico: Shore and Beach, v. 63, p. 18–28.

Thieler, E.R., Rodríguez, R.W., and Himmelstoss, E.A., 2007, Historical shoreline changes at Rincón, Puerto Rico, 1936–2006: U.S. Geological Survey Open-File Report 2007–1017, 32 p., accessed June 1, 2025, at https://doi.org/10.3133/ofr20071017.

Turner, I., Harley, M., Short, A., Simmons, J., Bracs, M., Phillips, M., and Splinter, K., 2016, A multi-decade dataset of monthly beach profile surveys and inshore wave forcing at Narrabeen, Australia: Scientific Data, v. 3, 13 p., accessed June 1, 2025, at https://doi.org/10.1038/sdata.2016.24.

U.S. Army Corps of Engineers, 1984, Shore protection manual: Department of the Army, Waterways Experiment Station, Corps of Engineers, Coastal Engineering Research Center, accessed September 15, 2025, at https://usace.contentdm.oclc.org/digital/collection/p16021coll11/id/1934/.

U.S. Geological Survey, 1976, Geologic history of Cape Cod: Massachusetts: U.S. Geological Survey General Interest Publication, accessed September 26, 2025, at https://doi.org/10.3133/7000013.

U.S. Geological Survey, 2020a, Landsat 4-5 Thematic Mapper Level-2, Collection 2: U.S. Geological Survey dataset, accessed June 1, 2025, at https://doi.org/10.5066/P9IAXOVV.

U.S. Geological Survey, 2020b, Landsat 7 Enhanced Thematic Mapper Plus Level-2, Collection 2: U.S. Geological Survey dataset, accessed June 1, 2025, at https://doi.org/10.5066/P9C7I13B.

U.S. Geological Survey, 2020c, Landsat 8-9 Operational Land Imager / Thermal Infrared Sensor Level-2, collection 2: U.S. Geological Survey dataset, accessed June 1, 2025, at https://doi.org/10.5066/P9OGBGM6.

Vitousek, S., Buscombe, D., Vos, K., Barnard, P.L., Ritchie, A.C., and Warrick, J.A., 2023a, The future of coastal monitoring through satellite remote sensing: Cambridge Prisms: Coastal Futures, v. 1, accessed June 1, 2025, at https://doi.org/10.1017/cft.2022.4.

Vitousek, S., Vos, K., Splinter, K.D., Erikson, L., and Barnard, P.L., 2023b, A model integrating satellite-derived shoreline observations for predicting fine-scale shoreline response to waves and sea-level rise across large coastal regions: Journal of Geophysical Research. Earth Surface, v. 128, no. 7, accessed June 1, 2025, at https://doi.org/10.1029/2022JF006936.

Vitousek, S., Vos, K., Splinter, K.D., Parker, K., O'Neill, A., Foxgrover, A., Hayden, M., Thomas, J., Erikson, L., and Barnard, P., 2024, Scalable, data-assimilated models predict large-scale shoreline response to waves and sea-level rise: Scientific Reports, v. 14, 12 p., accessed June 1, 2025, at https://doi.org/10.1038/s41598-024-77030-4.

Vos, K., Harley, M.D., Splinter, K.D., Simmons, J.A., and Turner, I.L., 2019a, Sub-annual to multi-decadal shoreline variability from publicly available satellite imagery: Coastal Engineering, v. 150, p. 160–174, accessed June 1, 2025, at https://doi.org/10.1016/j.coastaleng.2019.04.004.

Vos, L., Splinter, K.D., Harley, M.D., Simmons, J.A., and Turner, I.L., 2019b, CoastSat—A Google Earth Engine-enabled Python toolkit to extract shorelines from publicly available satellite imagery: Environmental Modelling & Software, v. 122, 7 p., accessed June 1, 2025, at https://doi.org/10.1016/j.envsoft.2019.104528.

Vos, K., Splinter, K.D., Palomar-Vázquez, J., Pardo-Pascual, J., Almonacid-Caballer, J., Cabezas-Rabadan, C., Kras, E., Luijendijk, A., Calkoen, F., Almeida, L., Pais, D., Klein, A., Mao, Y., Harris, D., Castelle, B., Buscombe, D., and Vitousek, S., 2023, Benchmarking satellite-derived shoreline mapping algorithms: Communications Earth & Environment, v. 4, 17 p., accessed June 1, 2025, at https://doi.org/10.1038/s43247-023-01001-2.

Vos, K., Harley, M. D., Splinter, K. D., Walker, A. and Turner, I. L., 2020, Beach slopes from satellite-derived shorelines: Geophysical Research Letters, v. 47, accessed June 1, 2025, at https://doi.org/10.1029/2020GL088365.

Warrick, J.A., George, D.A., Gelfenbaum, G., Ruggiero, P., Kaminsky, G., and Beirne, M., 2009, Beach morphology and change along the mixed grain-size delta of the dammed Elwha River, Washington: Geomorphology, v. 111, no. 3–4, p. 136–148, accessed June 1, 2025, at https://doi.org/10.1016/j.geomorph.2009.04.012.

Warrick, J.A., Stevens, A.W., Miller, I.M., Harrison, S.R., Ritchie, A.C., and Gelfenbaum, G., 2019, World's largest dam removal reverses coastal erosion: Scientific Reports, v. 9, 12 p., accessed June 1, 2025, at https://doi.org/10.1038/s41598-019-50387-7.

Warrick, J.A., Vos, K., East, A.E., and Vitousek, S., 2022, Fire (plus) flood (equals) beach—Coastal response to an exceptional river sediment discharge event: Scientific Reports, v. 12, 15 p., accessed June 1, 2025, at https://doi.org/10.1038/s41598-022-07209-0.

Warrick, J.A., Vos, K., Buscombe, D., Ritchie, A.C., and Curtis, J.A., 2023, A large sediment accretion wave along a northern California littoral cell: Journal of Geophysical Research. Earth Surface, v. 128, no. 7, accessed June 1, 2025, at https://doi.org/10.1029/2023JF007135.

Warrick, J.A., Buscombe, D., Vos, K., Kenyon, H., Ritchie, A.C., Harley, M.D., Janda, C., L'Heureux, J., and Vitousek, S., 2025, Shoreline seasonality of California's beaches: Journal of Geophysical Research. Earth Surface, v. 130, no. 2, accessed June 1, 2025, at https://doi.org/10.1029/2024JF007836.

Xu, H., 2006, Modification of normalised difference water index (NDWI) to enhance open water features in remotely sensed imagery: International Journal of Remote Sensing, v. 27, no. 14, p. 3025–3033, accessed June 1, 2025, at https://doi.org/10.1080/01431160600589179.

Glossary

CoastSat An open-source software toolkit that allows users to retrieve time-series of shoreline positions derived from publicly available satellite imagery.

CoastSeg An interactive browser-based program with an easy-to-use graphical interface and tools for obtaining satellite-derived shorelines. CoastSeg has the option to use different workflows to obtain shorelines from satellite imagery: the CoastSat workflow, and another workflow that uses deep learning.

CoastSeg:CoastSat The re-implementation of CoastSat methods within the CoastSeg platform, used in this study.

FES2014 A Finite Element Solution tide model developed in 2014–16.

Geographical Java Script Object Notation (GeoJSON) An open-format file for representing geographical features and with other non-spatial attributes.

in situ shorelines Traditionally sourced shorelines from various data sources and methods outlined in section 3.0, including lidar, Global Navigation Satellite System (GNSS), and manually digitized shorelines from imagery.

Satellite-derived shorelines (SDS) Shorelines automatically derived from satellite imagery using a variety of methods and workflows.

Surveying wide-area shorelines (SWASH) Intensive shoreline data collection effort that took place in Cape Cod, Massachusetts from 1998–2005.

For additional information contact:

Director, Pacific Coastal and Marine Science Center
U.S. Geological Survey
2885 Mission Street,
Santa Cruz, California 95060

or visit our website at
https://www.usgs.gov/centers/pcmsc

Publishing support provided by the U.S. Geological Survey, Science Publishing Network, Baltimore Publishing Service Center

ISSN 2331-1258 (online)
https://doi.org/10.3133/ofr20251054